A diffuse domain method for two-phase flows with large density ratio in complex geometries

Zhenlin Guo[1,2,†], **Fei Yu**[2], **Ping Lin**[3], **Steven Wise**[4] **and John Lowengrub**[2]

[1]Mechanics Division, Beijing Computational Science Research Center, Building 9, East Zone, ZPark II, No. 10 East Xibeiwang Road, Haidian District, Beijing 100193, PR China

[2]Department of Mathematics, University of California, Irvine, CA 92697, USA

[3]Department of Mathematics, University of Dundee, Dundee DD1 4HN, UK

[4]Department of Mathematics, University of Tennessee, Knoxville, TN 37996, USA

We present a quasi-incompressible Navier–Stokes–Cahn–Hilliard (q-NSCH) diffuse interface model for two-phase fluid flows with variable physical properties that maintains thermodynamic consistency. Then, we couple the diffuse domain method with this two-phase fluid model – yielding a new q-NSCH-DD model – to simulate the two-phase flows with moving contact lines in complex geometries. The original complex domain is extended to a larger regular domain, usually a cuboid, and the complex domain boundary is replaced by an interfacial region with finite thickness. A phase-field function is introduced to approximate the characteristic function of the original domain of interest. The original fluid model, q-NSCH, is reformulated on the larger domain with additional source terms that approximate the boundary conditions on the solid surface. We show that the q-NSCH-DD system converges to the q-NSCH system asymptotically as the thickness of the diffuse domain interface introduced by the phase-field function shrinks to zero ($\epsilon \to 0$) with $\mathcal{O}(\epsilon)$. Our analytic results are confirmed numerically by measuring the errors in both L^2 and L^∞ norms. In addition, we show that the q-NSCH-DD system not only allows the contact line to move on curved boundaries, but also makes the fluid–fluid interface intersect the solid object at an angle that is consistent with the prescribed contact angle.

Key words: multiphase flow, contact lines, computational methods

1. Introduction

Multiphase flows in complex geometries have many applications in the physical and biological sciences. To numerically simulate such physical phenomena involves solving interfacial problems with complex geometries and moving contact lines that separate fluid components at solid boundaries. In addition, special treatment of the contact line is needed to regularize the stress singularity. These are highly challenging problems for numerical simulation. Using standard discretization methods to solve these problems requires a triangulation of the complicated domain and thus rules out coarse-scale discretizations and with it efficient multilevel solutions. Many numerical methods have been developed for

† Email address for correspondence: elpharay@gmail.com

solving multiphase flows in complex geometries. Examples are fictitious domain methods (Glowinski *et al.* 2001; Zhang *et al.* 2018), extended finite element methods (Fries & Belytschko 2010), immersed boundary methods (Schneider 2015; Stein, Guy & Thomases 2017), immersed interface methods (Li 2003; Chen, Li & Lin 2007; Gong *et al.* 2018; O'Brien & Bussmann 2018) and the volume penalty method (Shirokoff & Nave 2014; De Stefano, Nejadmalayeri & Vasilyev 2016), where the complex geometry is embedded in a larger, regular domain with a test function being used to enforce the boundary conditions at solid–fluid interfaces. Other methods include boundary integral methods (Biros, Ying & Zorin 2004; Mittal *et al.* 2008), which explicitly incorporate the boundary conditions in the reformulated equations, front-tracking methods (Tryggvason *et al.* 2001; Zolfaghari, Izbassarov & Muradoglu 2017) and arbitrary Eulerian–Lagrangian methods (Hu, Patankar & Zhu 2001; Gilmanov & Sotiropoulos 2005; Anjos *et al.* 2013) that utilize a separate Lagrangian mesh to track the complex boundary and either smear the boundary conditions across several mesh points or explicitly enforce the boundary conditions on the Lagrangian mesh that cuts across the Eulerian mesh using body forces or modified discretizations. Methods along these lines include level-set, ghost-fluid, volume of fluid/level-set and cut-cell methods (Kirkpatrick, Armfield & Kent 2003; Gao *et al.* 2007; Herrmann 2008; de Zélicourt *et al.* 2009; Zhang & Ni 2014; Gutiérrez *et al.* 2018; Cao *et al.* 2019). However, most of these methods require modifications of standard finite element or finite difference software packages.

The diffuse domain (DD) method was proposed in Li *et al.* (2009) to solve partial differential equations in stationary/moving complex geometries with Dirichlet, Neumann or Robin boundary conditions. In this method, the complex geometry is extended to a larger, regular domain and a phase-field function is used to smoothly approximate the characteristic function of the original domain. The original partial differential equation is then reformulated on the larger domain with additional source terms that approximate the boundary conditions. It has been shown that the reformulated partial differential equation asymptotically converges to the original system as the width of the diffuse interface layer tends to zero (Li *et al.* 2009; Yu, Chen & Thornton 2012; Lervag & Lowengrub 2015; Chadwick *et al.* 2018; Poulsen & Voorhees 2018; Yu, Guo & Lowengrub 2020). The advantages of such a method are that no modifications of standard software packages are required and the stationary/moving complex boundary can be imposed easily and smoothly.

The DD method has recently been coupled with a standard two-phase diffuse interface model to study two-phase fluid flows in complex geometries (Aland, Lowengrub & Voigt 2010), where the fluid model is restricted to the case that the densities and viscosities of the two fluids are exactly the same. Phase-field, or diffuse interface, models have now emerged as a powerful method to simulate many types of multiphase flows (Guo, Lin & Lowengrub 2014*a*; Guo, Lin & Wang 2014*b*; Guo & Lin 2015; Jiang *et al.* 2015; Zhang & Wang 2016; Guo *et al.* 2017). The basic idea is to introduce a phase variable (order parameter) that varies continuously over thin interfacial layers and is mostly uniform in the bulk phases. In this way the phase variable can characterize different fluid component regions. Sharp interfaces are replaced by thin transition regions with non-zero thickness. One set of governing equations for the whole computational domain can be derived using variational techniques with respect to a free energy. The order parameter fields satisfy an advection–diffusion equation (usually the advective Cahn–Hilliard equations) and are coupled to Navier–Stokes-type equations through extra reactive stresses that mimic surface tension.

The classical phase-field model, Model H (Hohenberg 1977), was initially developed for simulating a binary incompressible fluid with density-matched components, and was later

generalized for simulating binary incompressible fluids with variable density components (Boyer 2002; Ding, Spelt & Shu 2007; Abels, Garcke & Grun 2012; Dong & Shen 2012; Aki *et al.* 2014; Gong, Zhao & Wang 2017; Gong *et al.* 2018; Shokrpour Roudbari *et al.* 2018). Some of these models, however, do not satisfy Galilean invariance, local mass conservation or are not thermodynamically consistent. A challenge is maintaining local mass conservation, thermodynamic consistency and Galilean invariance. In Lowengrub & Truskinovsky (1998), Model H was extended to a thermodynamically consistent model for variable density flows using the mass concentration as the phase variable and the mass-averaged velocity as the velocity field. Moreover, the fluids mix at the interfacial region which generates changes in the density even if the fluid components are incompressible individually. Such a system was called quasi-incompressible and leads to a (generally) non-solenoidal velocity field ($\nabla \cdot \boldsymbol{v} \neq 0$) and an extra pressure term appears in the Cahn–Hilliard equation compared to Model H. More recently, two other quasi-incompressible phase-field models (Gong *et al.* 2017; Shokrpour Roudbari *et al.* 2018) were developed to study binary fluids with variable densities, where the volume fraction was employed as the phase variable and a different free energy was used for the model derivations.

In this paper, we couple the DD method and a two-phase diffuse interface model to simulate binary flow in complex geometries. In particular, we first develop a thermodynamically consistent diffuse interface model, which we refer to as the quasi-incompressible Navier–Stokes Cahn–Hilliard model (q-NSCH), that allows for large density and viscosity differences between the two fluids. The model also employs the volume fraction as the phase variable. Compared to the models in Gong *et al.* (2017) and Shokrpour Roudbari *et al.* (2018), we use a different free energy and a different derivation framework that leads to a simple formulation of the system equations. We then combine the DD method with the q-NSCH system, namely the q-NSCH-DD model, to simulate two-phase flows in complex geometries. We perform a matched asymptotic analysis for the q-NSCH-DD model to show that it converges to the original q-NSCH model as the thickness of the DD interface shrinks to zero ($\epsilon \to 0$) with first-order accuracy, e.g. $O(\epsilon)$. We present several numerical tests that illustrate the flexibility and accuracy of the approach.

The outline of the paper is as follows. In § 2, we present our q-NSCH model and, in § 3, its DD reformulation (the q-NSCH-DD system). Appendix A shows the asymptotic analysis of the q-NSCH-DD model. The numerical method and its implementation are described in appendix B. In § 4, we show several numerical simulations and results. Finally in § 5, we share some parting thoughts about the work presented here.

2. Derivation of the q-NSCH model

Here we follow the thermodynamic framework in Guo & Lin (2015) and derive a new diffuse interface model for two-phase flows with variable density and viscosity. The model equations are derived through a variational procedure that guarantees thermodynamic consistency.

2.1. *Phase variable and variable density*

Suppose in a control volume V we have two fluids (labelled by $i = 1, 2$) that fill volumes V_i separately. The volume fraction for the ith fluid can be given by $c_i = V_i/V$. Further we assume that the two fluids can mix within an interfacial region separating the two fluids and the volume occupied by a given amount of mass of the single fluid does not change

after mixing. Therefore $c_1 + c_2 = 1$ within the control volume V. Given the total mass and volume for the mixture, $M = M_1 + M_2$ and $V = V_1 + V_2$, we introduce the actual local mass density ρ_i for each fluid, and the local volume-averaged mass density $\tilde{\rho}_i$ taken over a sufficient small volume V:

$$\rho_i = \frac{M_i}{V_i}, \quad \tilde{\rho}_i = \frac{M_i}{V} = \frac{M_i}{V_i}\frac{V_i}{V} = \rho_i c_i, \tag{2.1a,b}$$

where ρ_i is a positive constant. We then define the volume-averaged density of the mixture as

$$\rho = \tilde{\rho}_1 + \tilde{\rho}_2 = \rho_1 c_1 + \rho_2 c_2. \tag{2.2}$$

Since $c_1 + c_2 = 1$, we assume that the phase variable with respect to volume fraction is given by $c = c_1 = 1 - c_2$. The corresponding variable density for the mixture can be rewritten as

$$\rho = (\rho_1 - \rho_2)c + \rho_2. \tag{2.3}$$

Suppose that the two fluids move with different velocities $\boldsymbol{u}_i(\boldsymbol{x}, t)$, then mass conservation for the mixture is given by

$$\partial_t(\tilde{\rho}_1 + \tilde{\rho}_2) + \boldsymbol{\nabla} \cdot (\tilde{\rho}_1 \boldsymbol{u}_1 + \tilde{\rho}_2 \boldsymbol{u}_2) = 0. \tag{2.4}$$

The mass-averaged velocity $\boldsymbol{u} := (\tilde{\rho}_1 \boldsymbol{u}_1 + \tilde{\rho}_2 \boldsymbol{u}_2)/\rho$ and ρ, defined in (2.2), satisfy the mass conservation equation:

$$\partial_t \rho + \boldsymbol{\nabla} \cdot (\rho \boldsymbol{u}) = 0. \tag{2.5}$$

2.2. *Balance laws*

We next consider the balance laws for the two-fluid mixture. Suppose the two-phase fluid is combined in a domain Ω. We then take an arbitrary control volume $V(t) \subset \Omega$ that moves with the mixture. Within the control volume, we define the following quantities for the two-phase fluid:

$$M = \int_{V(t)} \rho \, dV, \tag{2.6}$$

$$\boldsymbol{P} = \int_{V(t)} \rho \boldsymbol{u} \, dV, \tag{2.7}$$

$$E = \int_{V(t)} \left(\frac{1}{2}\rho|\boldsymbol{u}|^2 + \tilde{\sigma}F(c) + \frac{\tilde{\sigma}\epsilon_c|\boldsymbol{\nabla}c|^2}{2} - \rho g z \right) dV, \tag{2.8}$$

$$C = \int_{V(t)} c \, dV, \tag{2.9}$$

where M, $\boldsymbol{P}$, E and C are the total mass, momentum, free energy and constituent volume of fluid 1 within the control volume $V(t)$. Further, $\rho(c)$ is the variable density of the mixture, $\boldsymbol{u}$ is the mass-averaged velocity of the mixture, $|\boldsymbol{u}|^2/2$ is the kinetic energy per unit mass, g is the gravitational constant, z is the vector in the vertical direction, $\tilde{\sigma}F(c) + \tilde{\sigma}\epsilon_c|\boldsymbol{\nabla}c|^2/2$ is the Cahn–Hilliard-type interfacial free energy, $F(c) = c^2(c-1)^2/4\epsilon_c$ is double-well potential, ϵ_c is a small parameter that characterizes the thickness of the diffuse interface separating the fluid components and $\tilde{\sigma}$ is the surface tension that is related to the physical

surface tension σ through $\sigma = 6\sqrt{2}\tilde{\sigma}$. The general forms of the physical balance laws associated with M, P, E and C can be given as follows:

$$\frac{dM}{dt} = 0, \tag{2.10}$$

$$\frac{dP}{dt} = \int_{\partial V(t)} \boldsymbol{m} \cdot \boldsymbol{n} \, dA - \int_{V(t)} \rho g z \, dV, \tag{2.11}$$

$$\frac{dE}{dt} = -\int_{\partial V(t)} \boldsymbol{q}_E \cdot \boldsymbol{n} \, dA + \int_{V(t)} D \, dV \quad (D \leqslant 0), \tag{2.12}$$

$$\frac{dC}{dt} = -\int_{\partial V(t)} \boldsymbol{q}_C \cdot \boldsymbol{n} \, dA, \tag{2.13}$$

where $\boldsymbol{m}$ is a tensor, $\boldsymbol{q}_E$ and $\boldsymbol{q}_C$ are fluxes and D is the dissipation function, which will be specified later. The mass balance (2.10) ensures (2.5) is satisfied. The momentum balance (2.11) leads to

$$\rho \frac{D\boldsymbol{u}}{Dt} = \nabla \cdot \boldsymbol{m} - \rho g z, \tag{2.14}$$

where $D/Dt = \partial_t + \boldsymbol{u} \cdot \nabla$. The constituent volume balance equation (2.13) gives that

$$\frac{Dc}{Dt} + c(\nabla \cdot \boldsymbol{u}) = -\nabla \cdot \boldsymbol{q}_C. \tag{2.15}$$

Further, by using the definition of ρ in (2.3) and the mass conservation (2.5), we obtain

$$\nabla \cdot \boldsymbol{u} = -\frac{1}{\rho} \frac{D\rho}{Dt} = -\frac{d\rho}{\rho \, dc} \frac{Dc}{Dt} = \frac{\rho_2 - \rho_1}{\rho} \frac{Dc}{Dt}. \tag{2.16}$$

Substituting Dc/Dt in (2.15), we obtain the quasi-incompressibility in the interfacial region for the two-phase flows:

$$\nabla \cdot \boldsymbol{u} = -\alpha \nabla \cdot \boldsymbol{q}_C, \tag{2.17}$$

where $\alpha = (\rho_2 - \rho_1)/\rho_2$.

We now consider the energy balance (2.12). We first take the time derivative of the free energy (2.8) to obtain

$$\frac{dE}{dt} = \int_{V(t)} \left\{ \rho \boldsymbol{u} \cdot \frac{D\boldsymbol{u}}{Dt} + (\tilde{\sigma} F'(c) - \tilde{\sigma} \epsilon_c \Delta c) \frac{Dc}{Dt} + \nabla \cdot \left(\tilde{\sigma} \epsilon_c \frac{Dc}{Dt} \nabla c \right) \right.$$
$$\left. -\tilde{\sigma} \epsilon_c (\nabla c \otimes \nabla c) : \nabla \boldsymbol{u} + \left(\tilde{\sigma} F(c) + \frac{\tilde{\sigma} \epsilon_c |\nabla c|^2}{2} \right) (\nabla \cdot \boldsymbol{u}) - \rho g \boldsymbol{u} \cdot \boldsymbol{z} \right\} dV, \tag{2.18}$$

where we have used the following identities:

$$\frac{D}{Dt} \left(F(c) + \frac{\epsilon_c |\nabla c|^2}{2} \right) = F'(c) \frac{Dc}{Dt} - \Delta c \frac{Dc}{Dt} + \nabla \cdot \left(\nabla c \frac{Dc}{Dt} \right)$$
$$- (\nabla c \otimes \nabla c) : \nabla \boldsymbol{u}, \tag{2.19}$$

$$\nabla c \cdot \frac{D}{Dt} \nabla c = \nabla c \cdot (\nabla c_t + \boldsymbol{u} \cdot \nabla (\nabla c)), \tag{2.20}$$

$$\nabla c \cdot \nabla c_t = \nabla \cdot (\nabla c c_t) - \Delta c c_t, \tag{2.21}$$

$$\nabla c \cdot (\boldsymbol{u} \cdot \nabla (\nabla c)) = \nabla \cdot (\nabla c (\boldsymbol{u} \cdot \nabla c)) - \Delta c (\boldsymbol{u} \cdot \nabla c) \\ - (\nabla c \otimes \nabla c) : \nabla \boldsymbol{u}. \tag{2.22}$$

Substituting $\rho (\mathrm{D}\boldsymbol{u}/\mathrm{D}t)$ and $\mathrm{D}c/\mathrm{D}t$ in (2.14) and (2.15), respectively, and applying the divergence theorem, we obtain

$$\frac{\mathrm{D}E}{\mathrm{D}t} = \int_{V(t)} \left\{ \nabla \cdot \left(\boldsymbol{m} \cdot \boldsymbol{u} + \tilde{\sigma}\epsilon_c \frac{\mathrm{D}c}{\mathrm{D}t}\nabla c \right) - (\boldsymbol{m}_0 + \tilde{\sigma}\epsilon_c(\nabla c \otimes \nabla c) + \tau) : \nabla \boldsymbol{u} \right. \\ - \left(-\tilde{\sigma}F(c) - \frac{\tilde{\sigma}\epsilon_c |\nabla c|^2}{2} + \left(\tilde{\sigma}F'(c) - \tilde{\sigma}\epsilon_c \Delta c \right) c \right) \nabla \cdot \boldsymbol{u} \\ \left. - \nabla \cdot \left(\tilde{\sigma} \left(F'(c) - \epsilon_c \Delta c \right) \boldsymbol{q}_C \right) + \boldsymbol{q}_C \cdot \nabla \left(\tilde{\sigma} \left(F'(c) - \epsilon_c \Delta c \right) \right) \right\} \mathrm{d}V \\ = \int_{V(t)} \left\{ \nabla \cdot \left(\boldsymbol{m} \cdot \boldsymbol{u} + \tilde{\sigma}\epsilon_c \frac{\mathrm{D}c}{\mathrm{D}t}\nabla c \right) - (\boldsymbol{m}_0 + \tilde{\sigma}\epsilon_c(\nabla c \otimes \nabla c)) : \boldsymbol{D}\boldsymbol{u} - \tau : \nabla \boldsymbol{u} \right. \\ - \left(\boldsymbol{m}_0 + \tilde{\sigma}\epsilon_c(\nabla c \otimes \nabla c) - \tilde{\sigma}F(c)\boldsymbol{I} - \frac{\tilde{\sigma}\epsilon_c |\nabla c|^2}{2}\boldsymbol{I} + \left(\tilde{\sigma}F'(c) - \tilde{\sigma}\epsilon_c \Delta c \right) c\boldsymbol{I} \right) : \frac{\boldsymbol{I}}{3}\nabla \cdot \boldsymbol{u} \\ \left. - \nabla \cdot \left(\tilde{\sigma} \left(F'(c) - \epsilon_c \Delta c \right) \boldsymbol{q}_C \right) + \boldsymbol{q}_C \cdot \nabla \left(\tilde{\sigma} \left(F'(c) - \epsilon_c \Delta c \right) \right) \right\} \mathrm{d}V, \tag{2.23}$$

where we denote the general stress tensor by $\boldsymbol{m} = \boldsymbol{m}_0 + \tau$, in which τ is the deviatoric stress tensor with zero trace, $\boldsymbol{m}_0$ is the unknown part to be defined later and $\boldsymbol{D}\boldsymbol{u} = \nabla \boldsymbol{u} - (\nabla \cdot \boldsymbol{u})\boldsymbol{I}/3$ is the deviatoric part of $\nabla \boldsymbol{u}$. Moreover, using the following identity and (2.17):

$$-\left(\boldsymbol{m}_0 + \tilde{\sigma}\epsilon_c(\nabla c \otimes \nabla c) - \tilde{\sigma}F(c)\boldsymbol{I} - \frac{\tilde{\sigma}\epsilon_c |\nabla c|^2}{2}\boldsymbol{I} + \left(\tilde{\sigma}F'(c)\epsilon_c - \tilde{\sigma}\epsilon_c \Delta c \right) c\boldsymbol{I} \right) : \frac{\boldsymbol{I}}{3}\nabla \cdot \boldsymbol{u} \\ = -\frac{1}{3}\left(\mathrm{tr}\,\boldsymbol{m}_0 - \frac{\tilde{\sigma}\epsilon_c |\nabla c|^2}{2} - 3\tilde{\sigma}F(c) + 3\left(\tilde{\sigma}F'(c) - \tilde{\sigma}\epsilon_c \Delta c \right) c \right) (\nabla \cdot \boldsymbol{u}) \\ = \frac{1}{3}\left(\mathrm{tr}\,\boldsymbol{m}_0 - \frac{\tilde{\sigma}\epsilon_c |\nabla c|^2}{2} - 3\tilde{\sigma}F(c) + 3\left(\tilde{\sigma}F'(c) - \tilde{\sigma}\epsilon_c \Delta c \right) c \right) \alpha\nabla \cdot \boldsymbol{q}_C \\ = \frac{1}{3}\nabla \cdot \left(\left(\mathrm{tr}\,\boldsymbol{m}_0 - \frac{\tilde{\sigma}\epsilon_c |\nabla c|^2}{2} - 3\tilde{\sigma}F(c) + 3\left(\tilde{\sigma}F'(c) - \tilde{\sigma}\epsilon_c \Delta c \right) c \right) \alpha\boldsymbol{q}_C \right) \\ - \frac{1}{3}\boldsymbol{q}_C \cdot \nabla \left(\left(\mathrm{tr}\,\boldsymbol{m}_0 - \frac{\tilde{\sigma}\epsilon_c |\nabla c|^2}{2} - 3\tilde{\sigma}F(c) + 3\left(\tilde{\sigma}F'(c) - \tilde{\sigma}\epsilon_c \Delta c \right) c \right) \alpha \right), \tag{2.24}$$

we define the pressure p as

$$-p = \frac{1}{3}\mathrm{tr}\,\boldsymbol{m} = \frac{1}{3}\left(\mathrm{tr}\,\boldsymbol{m}_0 - \frac{\tilde{\sigma}\epsilon_c |\nabla c|^2}{2} - 3\tilde{\sigma}F(c) + 3\left(\tilde{\sigma}F'(c) - \tilde{\sigma}\epsilon_c \Delta c \right) c \right), \tag{2.25}$$

such that

$$\boldsymbol{m}_0 = -\tilde{\sigma}\epsilon_c(\nabla c \otimes \nabla c) + \left(-p + \tilde{\sigma}F(c) + \frac{\tilde{\sigma}\epsilon_c |\nabla c|^2}{2} - \left(\tilde{\sigma}F'(c) - \tilde{\sigma}\epsilon_c \Delta c \right) c \right)\boldsymbol{I}. \tag{2.26}$$

Moreover, the term $(\boldsymbol{m}_0 + \tilde{\sigma}\epsilon_c(\nabla c \otimes \nabla c)) : \boldsymbol{D}\boldsymbol{u} = 0$ due to the above identity. By using (2.24), we rewrite (2.23) as

$$\frac{\mathrm{D}E}{\mathrm{D}t} = \int_{V(t)} \left\{ \nabla \cdot \left(\boldsymbol{m} \cdot \boldsymbol{u} + \tilde{\sigma}\epsilon_c \frac{\mathrm{D}c}{\mathrm{D}t} \nabla c \right) - \tau : \nabla \boldsymbol{u} - \nabla \cdot \left(\left(\tilde{\sigma}F'(c) - \epsilon_c \tilde{\sigma}\Delta c + \alpha p \right) \boldsymbol{q}_C \right) \right. $$

$$\left. + \boldsymbol{q}_C \cdot \nabla \left(\tilde{\sigma}F'(c) - \epsilon_c \tilde{\sigma}\Delta c + \alpha p \right) \right\} \mathrm{d}V, \tag{2.27}$$

$$\boldsymbol{q}_E = \boldsymbol{m} \cdot \boldsymbol{u} + \tilde{\sigma}\epsilon_c \frac{\mathrm{D}\phi}{\mathrm{D}t} \nabla c - \left(\tilde{\sigma}F'(c) - \epsilon_c \tilde{\sigma}\Delta c + \alpha p \right) \boldsymbol{q}_C, \tag{2.28}$$

$$D = -\tau : \nabla \boldsymbol{u} + \boldsymbol{q}_C \cdot \nabla \left(\tilde{\sigma}F'(c) - \epsilon_c \tilde{\sigma}\Delta c + \alpha p \right). \tag{2.29}$$

Therefore, to ensure the non-positivity of the dissipation term ($D \leqslant 0$, the second law of thermodynamics), we specify the unknown terms in the form

$$\tau = \nu(c)(\nabla \boldsymbol{u} + \nabla \boldsymbol{u}^T) - \tfrac{2}{3}\nu(c)(\nabla \cdot \boldsymbol{u})\boldsymbol{I}, \tag{2.30}$$

$$\boldsymbol{q}_C = -M(c)\nabla \left(\mu + \alpha p \right), \tag{2.31}$$

where $M(c) \geqslant 0$ is the mobility function, $\nu(c) = \nu_1 c + \nu_2(1 - c)$ is variable viscosity for the two-phase fluid and ν_i is the viscosity for the ith fluid, $\mu = \tilde{\sigma}F'(c) - \epsilon_c \tilde{\sigma}\Delta c$. Combining (2.29) and (2.30) we obtain

$$\boldsymbol{m} = \tau - \tilde{\sigma}\epsilon_c(\nabla c \otimes \nabla c) + \left(-p + \tilde{\sigma}F(c) + \frac{\tilde{\sigma}\epsilon_c|\nabla c|^2}{2} - c\mu \right) \boldsymbol{I}. \tag{2.32}$$

2.3. *Governing equations*

By substituting (2.30)–(2.32) in (2.14) and (2.15), and using the identity

$$\nabla \left(\tilde{\sigma}F(c) + \frac{\tilde{\sigma}\epsilon_c|\nabla c|^2}{2} - c\mu \right) = \tilde{\sigma}\epsilon_c \nabla \cdot (\nabla c \otimes \nabla c) - c\nabla \mu, \tag{2.33}$$

we obtain the q-NSCH system equations governing two-phase flows:

$$\rho \boldsymbol{u}_t + \rho \boldsymbol{u} \cdot \nabla \boldsymbol{u} = -\nabla p + \nabla \cdot (\nu(c)\nabla \boldsymbol{u}) + \tfrac{1}{3}\nabla (\nu(c)\nabla \cdot \boldsymbol{u}) + \mu \nabla c - \rho g z, \tag{2.34}$$

$$\nabla \cdot \boldsymbol{u} = \alpha \nabla \cdot (M(c)\nabla \mu) + \alpha^2 \nabla \cdot (M(c)\nabla p), \tag{2.35}$$

$$c_t + \nabla \cdot (\boldsymbol{u}c) = \nabla \cdot (M(c)\nabla \mu) + \alpha \nabla \cdot (M(c)\nabla p), \tag{2.36}$$

$$\mu = \tilde{\sigma}F'(c) - \epsilon_c \tilde{\sigma}\Delta c. \tag{2.37}$$

Here $M(c) = \sqrt{c^2(1 - c)^2}$ is the degenerate mobility, which becomes zero in the bulk regions ensuring that the velocity field is divergence free for single-phase flow. Moreover, the following boundary conditions on $\partial\Omega$ are imposed:

$$\boldsymbol{u} = \boldsymbol{u}_g \quad \text{(no slip)}, \tag{2.38}$$

$$\boldsymbol{n} \cdot \nabla(\mu + \alpha p) = 0 \quad \text{(no flux)}, \tag{2.39}$$

$$\boldsymbol{n} \cdot \nabla c = \frac{1}{\epsilon_c \sqrt{2}} \cos(\theta)(1 - c)c \quad \text{(contact angle)}. \tag{2.40}$$

Here $\boldsymbol{u}_g = (g_u, g_v)$ is the velocity on the boundary $\partial\Omega$ and $\boldsymbol{n}$ is the outward normal vector to Ω. Assuming $\partial\Omega$ is closed, the boundary velocity needs to satisfy $\int_{\partial\Omega} \boldsymbol{u}_g \cdot \boldsymbol{n} \, \mathrm{d}S = 0$.

Further, the contact angle θ is the static contact angle between the fluid–fluid interface and the physical boundary. This form of the boundary condition (2.40) was derived in Jacqmin (1999) (see also Gránásy *et al.* (2007), Do-Quang & Amberg (2009) and Aland *et al.* (2010) in the context of the DD method). In particular, for an interface in equilibrium, a contact angle condition (Young's law) may be posed: $\cos(\theta) = ((\sigma_{2S} - \sigma_{1S})/\sigma)$, where θ is the (equilibrium) contact angle and σ_{iS} is the interfacial energy between the solid and component *i*. The contact angle characterizes the wettability of the surface with $\theta = 0$ denoting complete wetting. However, in the dynamical setting with the no-slip condition, the force needed to move a contact line is infinite making it necessary to regularize the system. Numerous methods have been implemented to regularize the problem including introducing a slip velocity, microscopic interactions, a precursor film or a diffuse interface.

Recently, two other quasi-incompressible two-fluid models have been presented in Gong *et al.* (2017) and Shokrpour Roudbari *et al.* (2018), where a different phase variable ϕ is introduced leading to a different Cahn–Hilliard free energy and different systems of equations. In the paper by Shokrpour Roudbari *et al.* (2018), in order to ensure the energy conservation for both the model equations and the corresponding numerical method, they introduced a dual-density form (two formulations of the variable density of the mixture) to the modelling framework. These two forms of the density appear in the model simultaneously and cannot be used interchangeably, leading to an extra mass conservation equation that needs to be solved along with the model equations. Our model equations are more compact and satisfy the energy conservation naturally. There is only one form of the variable density, and no extra mass conservation equation. In the paper by Gong *et al.* (2017), the modelling framework they follow is based on the free energy dissipation which means that the framework is mainly focused on the isothermal case. Our modelling framework is more general, as the total energy, free energy and entropy can be introduced to the system in a thermodynamically consistent way, so that we can derive more general models to simulate the non-isothermal case or two-phase flows with non-uniform surface tension (surface tension gradient induced by the gradient of temperature or concentration of surfactants). Moreover, in their modelling framework, they did not provide the specific formulation for the Cahn–Hilliard free energy, which shortens the model derivation. However, to ensure the mass conservation of the fluid mixture and each fluid component, a parameter '*B*' is introduced to the Cahn–Hilliard equation, serving as the coefficient of the mobility of the chemical potential. In their work, the calculation of '*B*' seems quite long and complicated, and the resulting '*B*' also makes the model equations more complicated compared to our model.

3. Diffuse domain reformulation: q-NSCH-DD

We next assume that the domain Ω has a complex boundary $\partial \Omega$. To solve the q-NSCH model (2.34)–(2.40) numerically, we extend the results in Aland *et al.* (2010) and propose a DD approximation of the q-NSCH model in a larger and simpler domain $\tilde{\Omega}$ (see figure 1). The q-NSCH-DD model is

$$\rho(\phi \boldsymbol{u})_t + \rho \boldsymbol{u} \cdot \boldsymbol{\nabla}(\phi \boldsymbol{u}) = -\phi \boldsymbol{\nabla} p + \phi \boldsymbol{\nabla} \cdot (\nu \boldsymbol{\nabla} \boldsymbol{u}) + \frac{1}{3}\phi \boldsymbol{\nabla}(\nu \boldsymbol{\nabla} \cdot \boldsymbol{u}) + \frac{\tilde{\sigma}}{\epsilon_c}\phi \mu \boldsymbol{\nabla} c - \phi \rho g \boldsymbol{z}$$
$$+ BC_{\boldsymbol{u}}, \tag{3.1}$$

$$\boldsymbol{\nabla} \cdot (\phi \boldsymbol{u}) = \boldsymbol{u}_g \cdot \boldsymbol{\nabla} \phi + \alpha \boldsymbol{\nabla} \cdot (M(c)\phi \boldsymbol{\nabla} \mu) + \alpha^2 \boldsymbol{\nabla} \cdot (M(c)\phi \boldsymbol{\nabla} p)$$
$$+ BC_{\mu,p}, \tag{3.2}$$

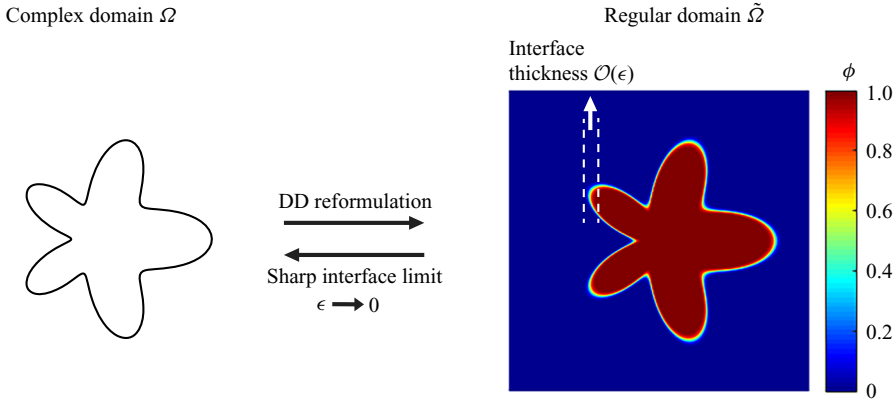Complex domain Ω Regular domain $\tilde{\Omega}$

FIGURE 1. Schematic of the DD method. The sharp (physical) interface domain Ω is embedded in a larger, square domain $\tilde{\Omega}$ where a phase-field function ϕ approximates the characteristic function of the deposition domain.

$$(\phi c)_t + \nabla \cdot (\phi c \boldsymbol{u}) = \nabla \cdot (\phi M(c) \nabla \mu) + \alpha \nabla \cdot (M(c) \phi \nabla p) + BC_{\mu,p}, \tag{3.3}$$

$$\phi \mu = \phi \epsilon_c F'(c) - \epsilon_c^2 \nabla \cdot (\phi \nabla c) + BC_c, \tag{3.4}$$

with the boundary conditions $\boldsymbol{u} = \boldsymbol{0}$, $\boldsymbol{n} \cdot \nabla c = \boldsymbol{n} \cdot \nabla(\mu + \alpha p) = 0$ on $\partial \tilde{\Omega}$. Note that the solution in Ω is insensitive to the boundary conditions on $\partial \tilde{\Omega}$ if $\partial \Omega$ and $\partial \tilde{\Omega}$ are sufficiently far apart (e.g. the distance between $\partial \Omega$ and $\partial \tilde{\Omega}$ is $\geqslant 10\epsilon$; Yu *et al.* (2020)). Here the DD function ϕ, given by

$$\phi(\boldsymbol{x}, t) = 0.5 \left(1 - \tanh\left(\frac{3r(\boldsymbol{x}, t)}{\epsilon}\right)\right), \tag{3.5}$$

is used to approximate the characteristic function of the original domain Ω. The function $r(\boldsymbol{x}, t)$ is the signed distance to $\partial \Omega$ ($r < 0$ inside Ω) and ϵ is the thickness of the DD boundary. We fix ϵ_c and let $\epsilon \to 0$ unless otherwise stated. The reformulated BC_* are used to enforce the original boundary conditions (2.38)–(2.40) on $\partial \Omega$. In particular,

$$BC_{\boldsymbol{u}} = -\frac{1 - \phi}{\epsilon^2}(\boldsymbol{u} - \boldsymbol{u}_g), \tag{3.6}$$

$$BC_{\mu,p} = 0, \tag{3.7}$$

$$BC_c = -\frac{\epsilon_c |\nabla \phi|}{\sqrt{2}} \cos(\theta)(1 - c)c. \tag{3.8}$$

Here, we extend $\boldsymbol{u}_g$ into $\tilde{\Omega}$ constantly in the normal direction. The advantage of the q-NSCH-DD system is that it is posed on a regular domain and can be solved by any standard approach (e.g. finite difference, finite element). In appendix A, we show that the q-NSCH-DD system (3.1)–(3.4) asymptotically converges to the original q-NSCH system (2.34)–(2.37) with boundary conditions (2.38)–(2.40) as $\epsilon \to 0$. Moreover, the numerical methods and the corresponding implementation are shown in appendix B.
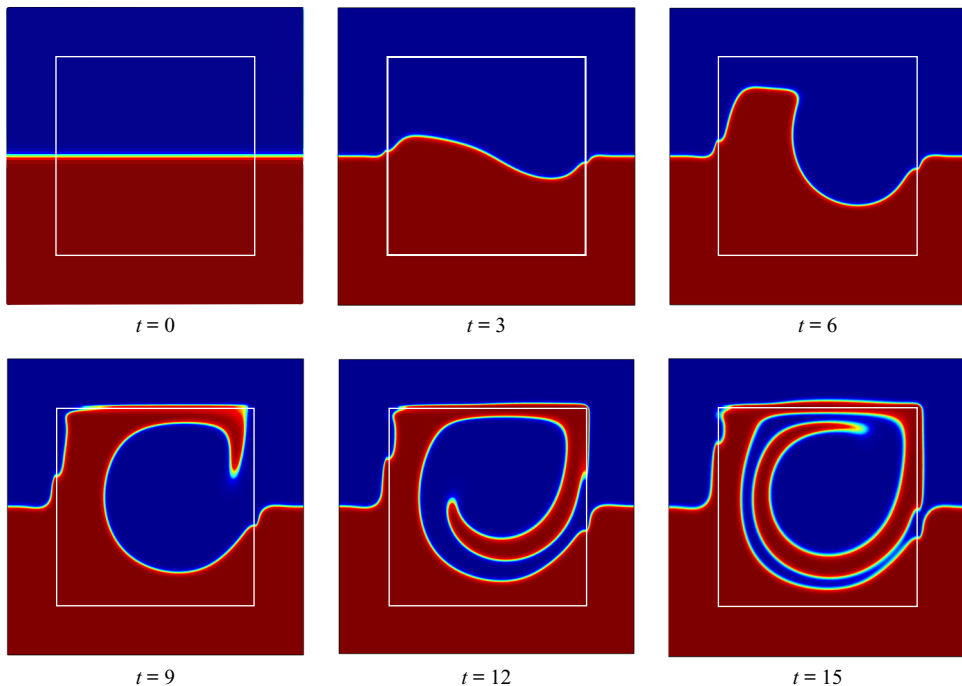
FIGURE 2. Evolution of the phase-field variable c in a cavity flow. The results are obtained using the q-NSCH-DD system with a grid size $h = 1.5/256$, $dt = 2.5 \times 10^{-3}$ and $\epsilon = 0.025$ in $\tilde{\Omega}$. The white box represents the physical domain Ω.

4. Numerical results

4.1. *Cavity flow*

We first consider a two-phase fluid flow in a driven cavity (Boyer 2002). The numerical results from the q-NSCH system (2.34)–(2.37) on the physical domain $\Omega = [0, 1]^2$ are compared to those from the q-NSCH-DD system (3.1)–(3.4) on an extended domain $\tilde{\Omega} = [-0.25, 1.25]^2$. For the original q-NSCH system, the boundary conditions on $\partial\Omega$ are imposed as

$$\boldsymbol{u} = \boldsymbol{u}_g, \tag{4.1}$$

$$\boldsymbol{n} \cdot \nabla(\mu + \alpha p) = 0, \tag{4.2}$$

$$\boldsymbol{n} \cdot \nabla c = 0, \tag{4.3}$$

where $\boldsymbol{u}_g = (g_u, g_v) = (g_u, 0)$, and

$$g_u = \begin{cases} \max\left(0, 1 - 4 \times (x - 0.5)^2\right), & y = 1 \\ 0, & y < 1. \end{cases} \tag{4.4}$$
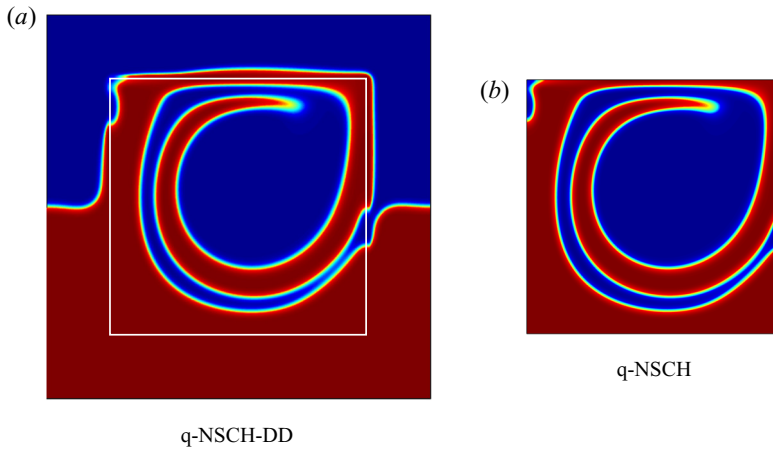
FIGURE 3. Comparisons between the phase-field variable obtained from the q-NSCH-DD system (*a*) and that from the q-NSCH system (*b*) at $t = 15$. The white box in (*a*) marks the physical domain Ω.

For the q-NSCH-DD system, the function ϕ, given by

$$\phi = 0.5 \left(1 + \tanh\left(\frac{3x}{\epsilon}\right)\right) \times 0.5 \left(1 + \tanh\left(\frac{3(1-x)}{\epsilon}\right)\right)$$
$$\times 0.5 \left(1 + \tanh\left(\frac{3y}{\epsilon}\right)\right) \times 0.5 \left(1 + \tanh\left(\frac{3(1-y)}{\epsilon}\right)\right), \qquad (4.5)$$

is used to approximate the characteristic function of Ω, and g_u is extended to $\tilde{\Omega}$ as follows:

$$g_u = \begin{cases} \max\left(0, 1 - 4 \times (x - 0.5)^2\right), & y \geqslant 1 - \epsilon \\ 0, & y < 1 - \epsilon. \end{cases} \qquad (4.6)$$

For both systems, the initial c is

$$c = \frac{1}{2}\left(1 - \tanh\left(\frac{0.5 - y}{2\sqrt{2}\epsilon_c}\right)\right), \qquad (4.7)$$

such that $c = 0$ for the fluid at the bottom and $c = 1$ for the top fluid. In addition, we set

$$\rho_1 = \rho_2 = 1, \quad \nu_1 = \nu_2 = 0.002, \quad g = 0, \quad \tilde{\sigma} = 0, \quad \theta = 90° \quad \text{and} \quad \epsilon_c = 0.05. \tag{4.8a-f}$$

We present the evolution of the phase-field variable c obtained from the q-NSCH-DD system in figure 2 and compare c at $t = 15$ with the one from the q-NSCH system at the same time in figure 3.

Moreover, we compare the results between the q-NSCH and q-NSCH-DD solutions to test the convergence of the q-NSCH-DD system as $\epsilon \to 0$. In particular, we use the results, including the velocities u_{exc}, v_{exc}, and phase variable c_{exc}, from the q-NSCH system with a grid size $h = 1/1024$ and a time step $dt = 3.90625 \times 10^{-5}$ as the exact solutions. For the q-NSCH-DD system, we obtain the corresponding numerical solutions u_ϵ, v_ϵ and c_ϵ using

ϵ	$E_u^{(2)}$	k	$E_v^{(2)}$	k	$E_c^{(2)}$	k
1.0×10^{-1}	5.17×10^{-2}	—	2.98×10^{-2}	—	1.09×10^{-2}	—
5.0×10^{-2}	2.40×10^{-2}	1.11	1.73×10^{-2}	0.78	4.25×10^{-3}	1.36
2.5×10^{-2}	1.12×10^{-2}	1.10	8.90×10^{-3}	0.96	1.75×10^{-3}	1.28
1.25×10^{-2}	5.46×10^{-3}	1.04	4.32×10^{-3}	1.04	7.50×10^{-4}	1.22
6.25×10^{-3}	2.72×10^{-3}	1.10	2.17×10^{-3}	0.99	3.21×10^{-4}	1.22

TABLE 1. The L^2 errors and convergence rate (k) of the velocities u, v and phase-field variable c with different values of ϵ in a cavity flow in §4.1. Here k stands for the convergence rate. See text for details.

ϵ	$E_u^{(\infty)}$	k	$E_v^{(\infty)}$	k	$E_c^{(\infty)}$	k
1.0×10^{-1}	2.05×10^{-1}	—	9.80×10^{-2}	—	3.65×10^{-2}	—
5.0×10^{-2}	1.22×10^{-1}	0.75	4.52×10^{-2}	1.12	1.47×10^{-2}	1.31
2.5×10^{-2}	6.64×10^{-2}	0.88	2.58×10^{-2}	0.81	6.12×10^{-3}	1.26
1.25×10^{-2}	3.44×10^{-2}	0.95	1.37×10^{-2}	0.91	2.66×10^{-3}	1.20
6.25×10^{-3}	1.74×10^{-2}	0.98	6.92×10^{-3}	0.99	1.15×10^{-3}	1.21

TABLE 2. The L^∞ errors and convergence rate (k) of the velocities u, v and phase-field variable c in a cavity flow in §4.1. Here k stands for the convergence rate. See text for details.

different values of ϵ, namely 0.1, 0.05, 0.025, 0.0125, 0.00625. We start with a grid size $h = 1.5/64$ and time step $dt = 10^{-2}$ and $\epsilon = 0.1$, and refine them together. For each ϵ, we restrict the solutions from q-NSCH-DD to the original domain Ω (see the smaller region bounded by the white solid line in figure 2) and compute the L^2 ($E^{(2)}$) and L^∞ ($E^{(\infty)}$) errors as

$$E_y^{(2)} = ||y_\epsilon - y_{exc}||_{L^2(\Omega)} \quad \text{and} \quad E_y^{(\infty)} = ||y_\epsilon - y_{exc}||_{L^\infty(\Omega)}, \qquad (4.9a,b)$$

where y_ϵ represents u_ϵ, v_ϵ, c_ϵ and y_{exc} represents u_{exc}, v_{exc}, c_{exc}. Note that $E_y^{(\infty)}$ is computed where $\phi \geqslant 0.5$. The errors at $t = 0.1$ are presented in tables 1 and 2. We observe that our DD approximation converges to the q-NSCH model with $\mathcal{O}(\epsilon)$.

Remark. Another choice of $BC_u = -\epsilon^{-3}(1 - \phi)(\boldsymbol{u} - \boldsymbol{u_g})$ was presented by Li *et al.* (2009) and later the scheme was shown to be $\mathcal{O}(\epsilon \ln(\epsilon))$ accurate by Yu *et al.* (2020). We here provide the numerical results using $BC_u = -\epsilon^{-3}(1 - \phi)(\boldsymbol{u} - \boldsymbol{u_g})$ for the cavity flow example in tables 3 and 4. This form of the velocity boundary condition was also used by Aland *et al.* (2010). The numerical set-up is identical to that considered above. We find that the errors are of a similar order of magnitude but are larger than those using $BC_u = -\epsilon^{-2}(1 - \phi)(\boldsymbol{u} - \boldsymbol{u_g})$ and are sub-first-order accurate, which is consistent with the results of Yu *et al.* (2020). In the following, we use $BC_u = -\epsilon^{-2}(1 - \phi)(\boldsymbol{u} - \boldsymbol{u_g})$ exclusively. Moreover, our numerical results agree with the convergence results shown in Franz *et al.* (2012).

ϵ	$E_u^{(2)}$	k	$E_v^{(2)}$	k	$E_c^{(2)}$	k
1.0×10^{-1}	4.23×10^{-2}	—	5.29×10^{-2}	—	8.09×10^{-2}	—
5.0×10^{-2}	1.54×10^{-2}	1.46	8.12×10^{-3}	2.70	1.43×10^{-3}	2.50
2.5×10^{-2}	7.57×10^{-3}	1.02	5.34×10^{-3}	0.60	5.04×10^{-4}	1.50
1.25×10^{-2}	5.63×10^{-3}	0.43	4.36×10^{-3}	0.29	6.25×10^{-4}	−0.31
6.25×10^{-3}	3.96×10^{-3}	0.51	3.24×10^{-3}	0.43	4.95×10^{-4}	0.34

TABLE 3. The L^2 errors and convergence rate (k) of the velocities u, v and phase-field variable c in a cavity flow using another choice of $BC_u = -\epsilon^{-3}(1 - \phi)(\boldsymbol{u} - \boldsymbol{u_g})$. See the remark in § 4.1 for details.

ϵ	$E_u^{(\infty)}$	k	$E_v^{(\infty)}$	k	$E_c^{(\infty)}$	k
1.0×10^{-1}	1.39×10^{-1}	—	6.97×10^{-1}	—	2.86×10^{-2}	—
5.0×10^{-2}	4.07×10^{-2}	1.77	1.73×10^{-1}	2.01	5.00×10^{-3}	2.52
2.5×10^{-2}	3.62×10^{-2}	0.17	1.88×10^{-1}	−0.12	2.03×10^{-3}	1.30
1.25×10^{-2}	3.11×10^{-2}	0.22	1.44×10^{-1}	0.38	2.39×10^{-3}	−0.24
6.25×10^{-3}	2.22×10^{-2}	0.49	3.45×10^{-2}	2.06	1.80×10^{-3}	0.41

TABLE 4. The L^∞ errors of the velocities u, v and phase-field variable c in a cavity flow using another choice of $BC_u = -\epsilon^{-3}(1 - \phi)(\boldsymbol{u} - \boldsymbol{u_g})$. See the remark in § 4.1 for details.

4.2. *Droplet spreading*

In order to test the accuracy of the q-NSCH-DD system with the moving contact line, we consider an example of a water droplet spreading on a flat substrate. In particular, we assume that there is a water droplet in the air, and is placed above a flat substrate. Due to the effect of gravity, the droplet falls down and spreads on the substrate. For the original q-NSCH system, the computational domain is $\Omega = [0, 1]^2$ with the following boundary conditions on $\partial \Omega$:

$$\boldsymbol{u} = 0 \quad \text{(no slip)}, \tag{4.10}$$

$$\boldsymbol{n} \cdot \nabla(\mu + \alpha p) = 0 \quad \text{(no flux)}, \tag{4.11}$$

$$\boldsymbol{n} \cdot \nabla c = \frac{1}{\epsilon_c \sqrt{2}} \cos(\theta)(1 - c)c \quad \text{(contact angle)}. \tag{4.12}$$

For the q-NSCH-DD system, we extend the computational domain to $\tilde{\Omega} = [-0.25, 1.25]^2$ with the following boundary conditions on $\partial \tilde{\Omega}$:

$$\boldsymbol{u} = 0 \quad \text{(no slip)}, \tag{4.13}$$

$$\boldsymbol{n} \cdot \nabla(\mu + \alpha p) = 0 \quad \text{(no flux)}, \tag{4.14}$$

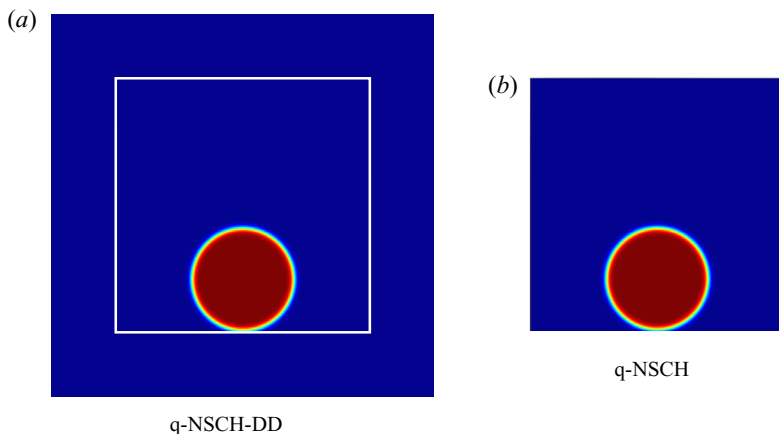$$\boldsymbol{n} \cdot \nabla c = 0 \quad \text{(no flux)}. \tag{4.15}$$

FIGURE 4. The computational domain for the q-NSCH-DD system (*a*) and the q-NSCH system (*b*), and the initial condition for phase variable *c*. The white box in (*a*) marks the physical domain Ω.

Moreover, we use the function ϕ, given by

$$\phi = 0.5 \left(1 + \tanh\left(\frac{3x}{\epsilon}\right)\right) \times 0.5 \left(1 + \tanh\left(\frac{3(1-x)}{\epsilon}\right)\right)$$
$$\times 0.5 \left(1 + \tanh\left(\frac{3y}{\epsilon}\right)\right) \times 0.5 \left(1 + \tanh\left(\frac{3(1-y)}{\epsilon}\right)\right), \quad (4.16)$$

to approximate the characteristic function of Ω. For both systems, the initial condition for the phase variable *c* is given by

$$c = \frac{1}{2}\left(1 - \tanh\left(\frac{r - 0.2}{2\sqrt{2}\epsilon_c}\right)\right), \quad (4.17)$$

with $r = \sqrt{(x - 0.5)^2 + (y - 0.21)^2}$, such that $c = 0$ for the water droplet and $c = 1$ for the air. In addition, we set

$$\left.\begin{array}{l} \rho_1 = 1, \quad \rho_2 = 1000, \quad \nu_1 = 0.1, \quad \nu_2 = 10, \quad g = 0.98, \quad \tilde{\sigma} = 10, \quad \theta = 60°, \\ \epsilon = 0.0025 \quad \text{and} \quad \epsilon_c = 0.005. \end{array}\right\} \quad (4.18)$$

In figure 4, we show the domains $\tilde{\Omega}$ and Ω together with the initial *c* for both systems. In figure 5, we show the dynamics of the contact line of the moving droplet, where the solid (dotted) lines represent the contour line ($c = 0.5$) of the numerical results obtained from the q-NSCH (the q-NSCH-DD) system. A good agreement can be observed between the two results. Again, we compare the results obtained from the two systems, and test the convergence rate of the q-NSCH-DD system as $\epsilon \to 0$. As in the previous section, we use the results of phase variable c_{exc} from the q-NSCH system with a grid size $h = 1/1024$ and a time step $dt = 3.90625 \times 10^{-5}$ as the exact solutions. For the q-NSCH-DD system, we obtain the corresponding numerical solutions c_ϵ using different values of ϵ, namely 0.1, 0.05, 0.025, 0.0125, 0.00625. We start with a grid size $h = 1.5/64$ and time step
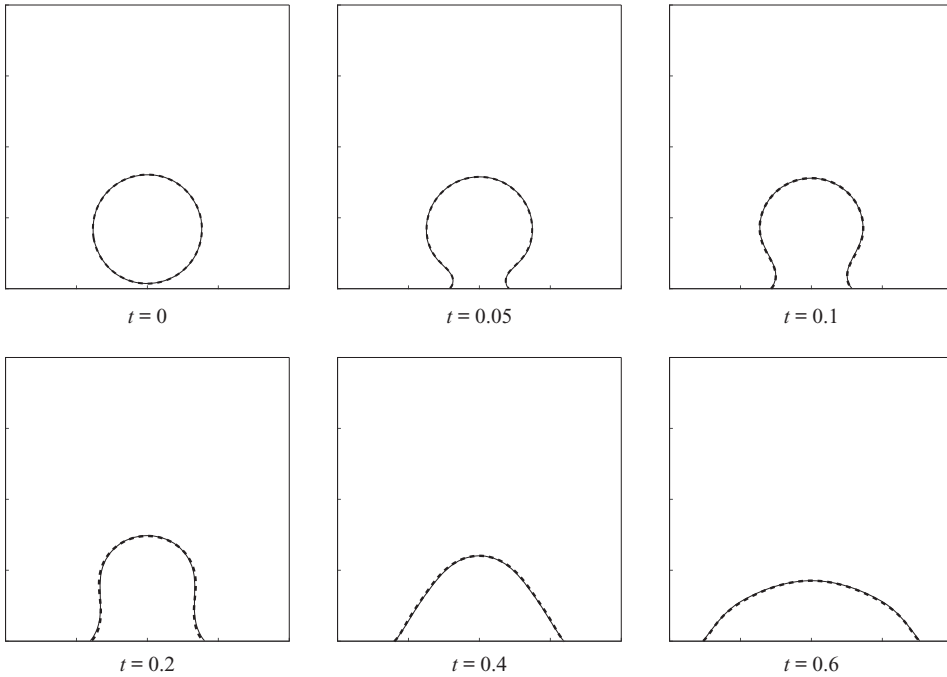
FIGURE 5. The dynamics of moving contact line of a water droplet on a solid substrate, where the solid (dotted) lines are the contour lines ($c = 0.5$) of the numerical results obtained from the q-NSCH (q-NSCH-DD) system.

$dt = 10^{-2}$ and $\epsilon = 0.1$, and refine them together. For each ϵ, we restrict the solutions from q-NSCH-DD to the original domain Ω and compute the L^2 ($E^{(2)}$) and L^∞ ($E^{(\infty)}$) errors as shown in (4.9*a,b*). The errors at $t = 0.1$ are presented in table 5, where we observe that our DD approximation converges to the q-NSCH system with $\mathcal{O}(\epsilon)$.

4.3. *Droplet on cylinder*

We next consider a circular droplet of diameter d wetting and dewetting on a solid cylinder. Initially, the droplet is placed on the cylinder of the same diameter d with contact angle $\theta_0 = 90°$ (see figure 6). We mention that careful studies for wetting and dewetting phenomena using a phase-field model have been presented in Gránásy *et al.* (2007), Dziwnik, Münch & Wagner (2017) and Rainer *et al.* (2019). With θ being the static contact angle, the contact line of the droplet recedes if $\theta < \theta_0$ or spreads if $\theta > \theta_0$, and eventually reaches an equilibrium with the interface intersecting the solid cylinder at an angle of θ. In the absence of gravity, the equilibrium state of the droplet can be obtained analytically by carving the cylinder out of a circle (Liu & Ding 2015; O'Brien & Bussmann 2018); see figure 7. The distance between the centres of the droplet and the cylinder, d_c, and the diameter of the circle, d_l, can be computed by solving

$$\pi d^2/4 = (\alpha + \theta)(d_l/2) - \alpha(d/2)^2 + (d_l d/4)\sin\theta, \tag{4.19}$$

$$d_l = d\cos\theta + \sqrt{d^2\cos^2\theta - d^2 + 4d_c^2}, \tag{4.20}$$

ϵ	$E_c^{(2)}$	k	$E_c^{(\infty)}$	k
2.0×10^{-2}	3.21×10^{-2}	—	1.13×10^{-1}	—
1.0×10^{-2}	1.29×10^{-2}	1.32	5.15×10^{-2}	1.30
5.0×10^{-3}	5.49×10^{-3}	1.23	2.21×10^{-2}	1.22
2.5×10^{-3}	2.42×10^{-2}	1.18	9.98×10^{-3}	1.15
1.25×10^{-3}	1.05×10^{-3}	1.20	4.47×10^{-3}	1.16

TABLE 5. The L^2 and L^∞ errors and convergence rate (k) of the phase-field variable restricted on Ω, ϕc, at time $t = 0.1$ with contact angle $\theta = 60°$. See § 4.2 for details.
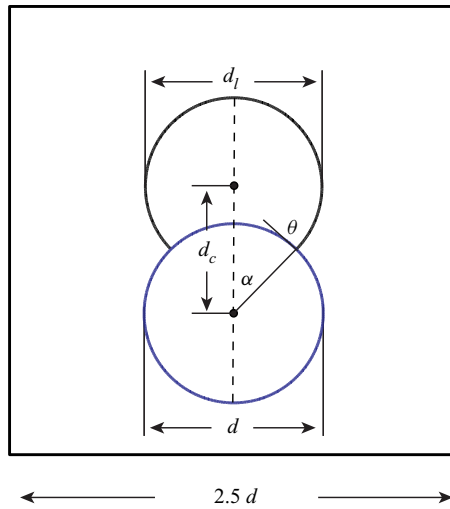
FIGURE 6. Set-up for droplet on cylinder.

where

$$\alpha = \arccos \left(\frac{d^2 + 4d_c^2 - d_l^2}{4dd_c} \right). \tag{4.21}$$

The exact solution c_{exc} is given by

$$c_{exc} = \frac{1}{2} \left(1 + \tanh \left(\frac{r_{exc} - 0.5d_l}{2\sqrt{2}\epsilon_c} \right) \right) \tag{4.22}$$

and $r_{exc} = \sqrt{(x - 1.25d)^2 + (y - 0.6d - d_c)^2}$. To apply the q-NCSH-DD system, we extend Ω to a larger domain $\tilde{\Omega} = [0, 2.5d] \times [0, 2.5d]$. The initial ϕ and c are given by

$$\left.\begin{aligned}
\phi &= \frac{1}{2} \left(1 + \tanh \left(\frac{3(r_\phi - 0.5d)}{\epsilon} \right) \right), \\
c &= \frac{1}{2} \left(1 + \tanh \left(\frac{r_c - 0.5d}{2\sqrt{2}\epsilon_c} \right) \right),
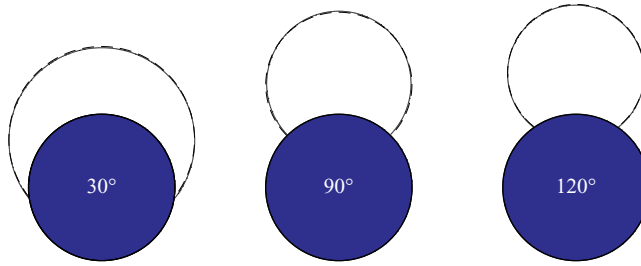\end{aligned}\right\} \tag{4.23}$$

FIGURE 7. Comparisons between the numerical results at equilibrium (solid lines) and the analytic solutions (dashed lines) with different static contact angles, where the angles are indicated inside the blue cylinders. See text for details.

ϵ	30°	k	90°	k	120°	k
2.0×10^{-2}	7.28×10^{-2}	—	1.09×10^{-1}	—	1.25×10^{-1}	—
1.0×10^{-2}	4.99×10^{-2}	0.55	6.85×10^{-2}	0.67	7.58×10^{-2}	0.72
5.0×10^{-3}	3.49×10^{-2}	0.52	4.64×10^{-2}	0.56	5.06×10^{-2}	0.58
2.5×10^{-3}	1.92×10^{-2}	0.86	2.51×10^{-2}	0.89	2.62×10^{-2}	0.95
1.25×10^{-3}	9.73×10^{-3}	0.98	1.26×10^{-2}	0.99	1.32×10^{-2}	0.99

TABLE 6. The L^2 errors and convergence rate (k) of the phase-field variable restricted on Ω, ϕc, at equilibrium with different static contact angles 30°, 90° and 120°.

where $r_\phi = \sqrt{(x - 1.25d)^2 + (y - 0.6d)^2}$ and $r_c = \sqrt{(x - 1.25d)^2 + (y - 0.6d - 0.5\sqrt{2}d)^2}$, such that $c = 1$ for the droplet (indicated by 1) and $c = 0$ for the surrounding fluid medium (indicated by 2). All the other parameters are set as follows:

$$\left.\begin{aligned} \rho_1 = 1000 \text{ (droplet)}, \quad \rho_2 = 1 \text{ (air)}, \quad \nu_1 = 0.1, \quad \nu_2 = 0.001, \quad \tilde{\sigma} = 1, \\ g = 0, \quad \epsilon_c = \epsilon, \quad d = 1. \end{aligned}\right\} \quad (4.24a\text{–}h)$$

We solve the q-NSCH-DD system with different values of ϵ $(= \epsilon_c)$ and various θ $(= 30°, 90°, 120°)$ to obtain the numerical solutions c at equilibrium and then compare with the corresponding analytical solutions c_{exc} in both L^2 and L^∞ norm:

$$E_c^{(2)} = ||c - c_{exc}||_{L^2(\Omega)} \quad \text{and} \quad E_c^{(\infty)} = ||c - c_{exc}||_{L^\infty(\Omega)}. \quad (4.25a,b)$$

We start with a grid size $h = 2.5/128$, a time step $dt = 0.01$ and $\epsilon = \epsilon_c = 0.02$ and conduct the error analysis by refining them together. In tables 6 and 7, we present the L^2 and L^∞ errors and find that our q-NSCH-DD system provides a first-order approximation to the exact solution (sharp interface).

In figure 7, we also present the numerical solutions ϕc with analytical solutions at equilibrium from the q-NSCH-DD system with various θ $(= 30°, 90°, 120°)$. The analytical solutions are the dashed curves. Here the grid size is $n = 2048$ and $\epsilon = \epsilon_c = 0.00125$. There is excellent agreement between the numerical and analytical solutions.

ϵ	30°	k	90°	k	120°	k
2.0×10^{-2}	2.93×10^{-1}	—	4.75×10^{-1}	—	5.61×10^{-1}	—
1.0×10^{-2}	2.09×10^{-1}	0.49	2.97×10^{-1}	0.68	3.51×10^{-1}	0.68
5.0×10^{-3}	1.46×10^{-1}	0.52	1.96×10^{-1}	0.60	2.32×10^{-1}	0.60
2.5×10^{-3}	8.39×10^{-2}	0.80	1.13×10^{-1}	0.79	1.22×10^{-1}	0.93
1.25×10^{-3}	4.34×10^{-2}	0.95	5.94×10^{-2}	0.93	6.19×10^{-2}	0.98

TABLE 7. The L^∞ errors of the phase-field variable restricted on Ω, ϕc, at equilibrium with different static contact angles 30°, 90° and 120°. See text for details.

4.4. *Penetration of a liquid droplet into porous media*

As a final test, we consider a two-dimensional droplet falling through a porous substrate consisting of three cylinders (C_i, $i = 1, 2, 3$) with different wettabilities, as shown in figure 8. We also fix the contact angle of the fluid–fluid interface at the walls to be 90°. The extended domain $\tilde{\Omega} = [0, 1] \times [0, 1]$ is discretized on a uniform mesh of [1024 × 1024]. The original physical domain is $\Omega = \tilde{\Omega}/(\cup C_i)$. There are three cylinders in the domain with radii $r_1 = 0.1$, $r_2 = 0.12$, $r_3 = 0.15$, and centres (0.3, 0.6), (0.4, 0.25), (0.7, 0.5), respectively. Initially, a heavy liquid drop with radius $r_d = 0.15$ is placed above the cylinders with the centre (0.5, 0.8). Note that the initial ϕ and c can be given by a slight modification of (4.23). Again, we let $c = 1$ stand for the heavy fluid droplet and $c = 0$ stands for the light fluid medium. All other parameters are set as follows:

$$\left. \begin{array}{l} \rho_1 = 1000, \quad \rho_2 = 1, \quad \nu_1 = 10, \quad \nu_2 = 0.1, \quad g = 1, \quad \tilde{\sigma} = 1, \\ \epsilon_c = 0.001, \quad \epsilon = 0.002. \end{array} \right\} \quad (4.26a\text{–}h)$$

The dynamics of droplet impact is shown in figure 8 via snapshots at different times. Initially, the droplet starts moving downwards due to gravitational forces. Dramatic deformations are observed when the droplet comes into contact with the left and right cylinders. After impacting on the cylinder at the bottom, the droplet splits into several parts. In the end, it is interesting to see that there is no liquid on the cylinders with contact angle of $\theta = 90°$ and $\theta = 120°$. All the liquid rests either on the cylinder with $\theta = 60°$ or on the walls.

4.5. *Moving domains*

In the next example, we simulate solid hydrophobic and hydrophilic balls impacting an air–water interface in two dimensions. The extended domain is $\tilde{\Omega} = [0, 1] \times [0, 1]$, and the air is placed on top of the water, with a flat interface at $y = 0.5$. Figure 9 shows the initial ϕ (the complex domain) and c (the air–water interface), which are given by

$$\left. \begin{array}{l} \phi = \dfrac{1}{2}\left(1 + \tanh\left(\dfrac{3(r_\phi - 0.1)}{\epsilon} \right) \right), \\ c = \dfrac{1}{2}\left(1 - \tanh\left(\dfrac{y - 0.5}{2\sqrt{2}\epsilon_c} \right) \right), \end{array} \right\} \quad (4.27)$$

where $r_\phi = \sqrt{(x - 0.5d)^2 + (y - 0.65d)^2}$ and such that $\phi = 0$ for the solid ball (in white) and $\phi = 0$ for the bulk regions with water (in red) or air (in blue). Here we assume that
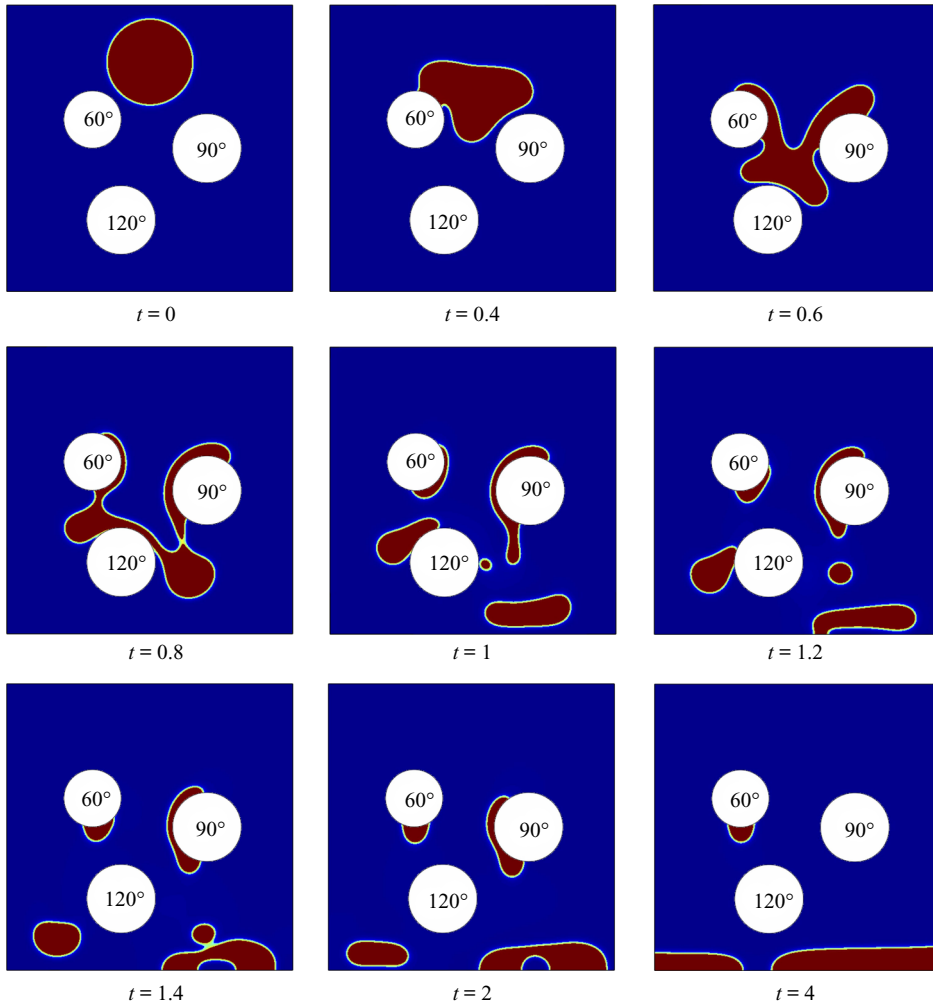
FIGURE 8. Snapshots of the penetration of a liquid droplet into porous media with different static contact angles, where the angles are indicated inside the white cylinders.

the ball moves with a constant velocity $\boldsymbol{v}_{ball} = (0, -1)$. All the other parameters are set as follows:

$$\left.\begin{array}{l}\rho_1 = 1000 \ (\text{water, lower fluid}), \quad \rho_2 = 1 \quad (\text{air, upper fluid}), \quad \nu_1 = 0.1, \\ \nu_2 = 0.001, \quad \tilde{\sigma} = 4, \quad g = 0.98, \quad \epsilon_c = \epsilon = 0.003.\end{array}\right\} \quad (4.28)$$

Two contact angle boundary conditions, namely $\theta_0 = 60°$ (hydrophilic) and $\theta_0 = 120°$ (hydrophobic), are imposed at the boundary of the solid ball. Figures 9 and 10 show the results of the simulations. For the hydrophilic ball, the contact line moves continuously on the surface of the ball until reaching the ball peak, at which the liquid merges and detaches from the surface of the ball. In contrast, for the hydrophobic ball, the contact line initially moves along the ball surface, but eventually rests on the ball. As a consequence of the pinned contact line, the length of the air cavity keeps growing. A neck then appears at the cavity and breaks up, thereby generating a bubble attached at the top of the ball.
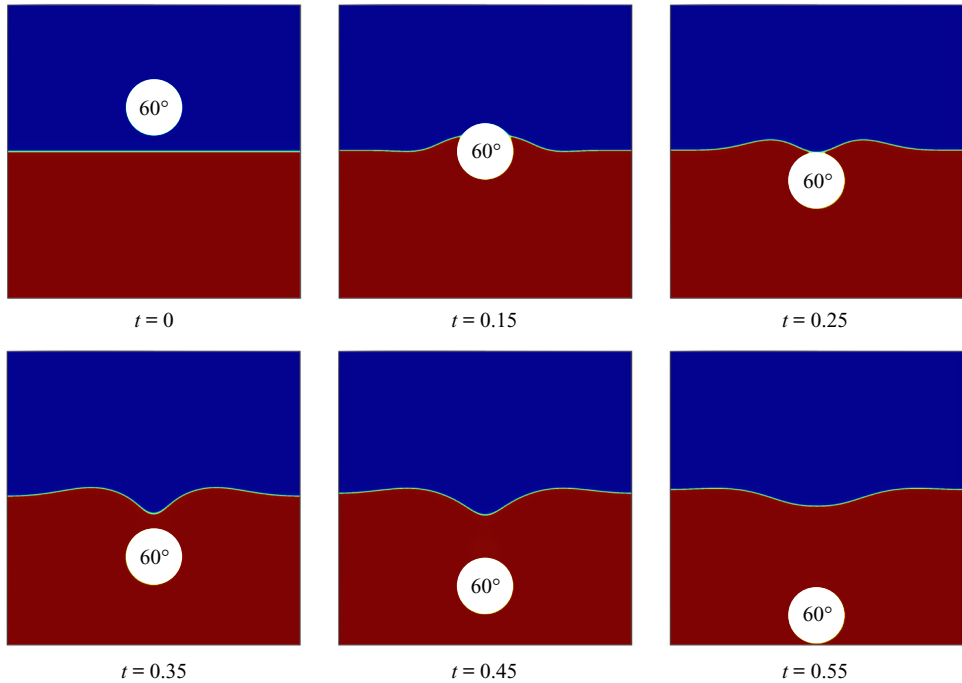
FIGURE 9. Snapshots of water entry of a hydrophilic ball with contact angle $60°$. Here the white region represents the solid falling ball, the blue region represents the air and the red region represents the water.

5. Discussion

A DD method was proposed to simulate two-phase flows with moving contact lines in complex geometries. We first derived a new thermodynamically consistent, locally mass conservative diffuse interface model, the q-NSCH system, for two-phase fluid flows with variable physical properties. We then combined this model with the DD method, to yield the q-NSCH-DD system in which a phase-field function ϕ was introduced to approximate the characteristic function of the original complex domain. Moreover, the q-NSCH-DD system contains extra source terms to enforce the boundary conditions on the complex domain. In the sharp interface limit, we showed that the q-NSCH-DD system converged to the q-NSCH system as the thickness ϵ of the DD boundary shrinks to zero at an $\mathcal{O}(\epsilon)$ rate.

We solved the q-NSCH-DD system using an existing finite difference multigrid solver on a staggered grid. Using the DD formulation, the system was solved on a larger, regular domain without any modification of the solver. Numerical results confirmed that the solution to the q-NSCH-DD system converged to that of the q-NSCH system and to analytical solutions. In addition, we showed that the q-NSCH-DD system not only allowed the contact line to move on the curved boundaries, but also made the fluid–fluid interface intersect the solid object at an angle consistent with the prescribed contact angle.

In Yu *et al.* (2020), the authors proposed that using a modified version of the boundary condition term $BC_u = -\epsilon^{-3}(1-\phi)(u - u_g - rn \cdot \nabla u)$, where r is the signed distance function to Ω, could achieve second-order accuracy in L^2 and 1.5-order accuracy in L^{∞}, although this was only shown to be the case in problems in Yu *et al.* (2020). In preliminary
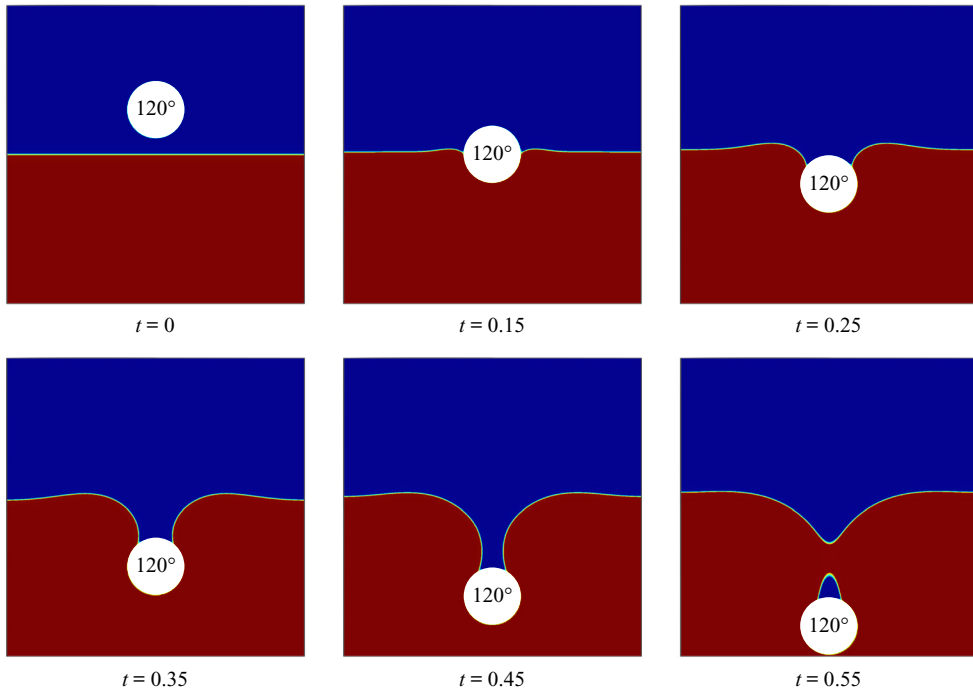
FIGURE 10. Snapshots of water entry of a hydrophobic ball with contact angle 120°. Here the white region represents the solid falling ball, the blue region represents the air and the red region represents the water.

work, we implemented this form of the boundary condition but did not find the expected improvement in convergence rate. This is likely due to the vector form of the problem, and the quasi-incompressibility condition, which couples the derivatives of the velocity. In future work, we will extend the asymptotic analysis in § 4 and use the approach developed in Yu *et al.* (2020) to guide the development of a higher-order-accurate version of the q-NSCH-DD system. Moreover, we will also consider dynamic contact angle formulations developed in Liu & Wu (2019). Since the DD formulation is dimension-independent, we also plan to develop a three-dimensional, spatially adaptive version of the solver.

Declaration of interests

The authors report no conflict of interest.

Appendix A. Asymptotic analysis of q-NSCH-DD

We use the method of matched asymptotic expansions to analyse the q-NSCH-DD system. In particular, we expand the variables in powers of the interface thickness in regions close to and far from the boundary. Parameter Y represents u, c, μ or p. The two expansions are then matched in a region where both are valid. We assume $\partial\Omega$ is smooth, but we are able to compute solutions accurately even if $\partial\Omega$ has corners.

A.1. *Outer expansions*

On each side far from the domain boundary $\partial\Omega$, there exists an outer expansion, here labelled $\bar{Y}_1(x; \epsilon)$ where $r < 0$ and $\phi = 1$ (e.g. inside Ω), and $\bar{Y}_2(x; \epsilon)$ where $r > 0$ and $\phi = 0$ (e.g. outside Ω), where $\bar{Y}_i$ represents $\bar{u}_i$, $\bar{c}_i$, $\bar{\mu}_i$ or $\bar{p}_i$. The outer expansion is away from $\partial\tilde{\Omega}$. On the boundary of $\partial\tilde{\Omega}$, we assume the following boundary conditions: $n \cdot \nabla\bar{u}_2 = 0$ and $n \cdot \nabla\bar{p}_2 = n \cdot \nabla\bar{\mu}_2 = n \cdot \nabla\bar{c}_2 = 0$. We assume the outer solution Y_1 has a regular expansion

$$\bar{Y}_1(x; \epsilon) = \bar{Y}_1^{(0)}(x) + \epsilon\bar{Y}_1^{(1)}(x) + \cdots, \quad i = 1, 2. \tag{A 1}$$

Plugging into (3.1)–(3.4), we obtain

$$\rho(c^{(0)})\frac{\partial}{\partial_t}\bar{u}_1^{(0)} + \rho(c^{(0)})\bar{u}_1^{(0)} \cdot \nabla\bar{u}_1^{(0)} = -\nabla\bar{p}_1^{(0)} + \nabla \cdot (\nu\nabla\bar{u}_1^{(0)}) + \frac{1}{3}\nabla(\nu\nabla \cdot \bar{u}_1^{(0)})$$
$$+ \frac{\tilde{\sigma}}{\epsilon_c}\bar{\mu}_1^{(0)}\nabla\bar{c}_1^{(0)} - \rho gz, \tag{A 2}$$

$$\nabla \cdot \bar{u}_1^{(0)} = \alpha\nabla \cdot (M(\bar{c}_1^{(0)})\nabla\bar{\mu}_1^{(0)}) + \alpha^2\nabla \cdot (M(\bar{c}_1^{(0)})\nabla\bar{p}_1^{(0)}), \tag{A 3}$$

$$\frac{\partial}{\partial_t}\bar{c}_1^{(0)} + \bar{u}_1^{(0)} \cdot \nabla\bar{c}_1^{(0)} = \nabla \cdot \left(M(\bar{c}_1^{(0)})\nabla\bar{\mu}_1^{(0)}\right) + \alpha\nabla \cdot \left(M(\bar{c}_1^{(0)})\nabla\bar{p}_1^{(0)}\right), \tag{A 4}$$

$$\bar{\mu}_1^{(0)} = \epsilon_c F'(\bar{c}_1^{(0)}) - \epsilon_c^2\nabla \cdot (\nabla\bar{c}_1^{(0)}). \tag{A 5}$$

Now, if $\bar{u}_1^{(0)}$, $\bar{p}_1^{(0)}$, $\bar{\mu}_1^{(0)}$ and $\bar{c}_1^{(0)}$ satisfy the corresponding boundary conditions on $\partial\Omega$ so that they are the unique solutions to q-NSCH (2.34)–(2.37), then the q-NSCH-DD system recovers the q-NSCH model at leading order. Assuming a similar expansion for $\bar{Y}_2$, we obtain $\bar{u}_2 = u_g$, $n \cdot \nabla\bar{p}_2 = n \cdot \nabla\bar{\mu}_2 = n \cdot \nabla\bar{c}_2 = 0$. The boundary conditions at $\partial\Omega$ are obtained by matching the outer and inner expansions.

A.2. *Inner expansions*

For the inner expansions, we introduce a local coordinate system near the domain boundary $\partial\Omega$:

$$x(s, z; \epsilon) = X(s; \epsilon) + \epsilon zn(s; \epsilon), \tag{A 6}$$

where $X(s; \epsilon)$ is a parametrization of the interface, $\boldsymbol{n}(s; \epsilon)$ is the interface normal vector that points out of Ω, $\boldsymbol{s}$ is the tangential vector and z is the stretched variable given by

$$z = \frac{r(\boldsymbol{x})}{\epsilon}, \tag{A7}$$

where $r(\boldsymbol{x})$ is the signed distance function to $\partial\Omega$. Note that $\lim_{z \to -\infty} \phi = 1$ and $\lim_{z \to +\infty} \phi = 0$. In the local coordinate system, the derivatives become

$$\boldsymbol{\nabla} = \frac{1}{\epsilon} \boldsymbol{n} \partial_z + \frac{1}{1 + \epsilon z \kappa} \boldsymbol{\nabla}_s, \tag{A8}$$

$$\Delta = \frac{1}{\epsilon^2} \partial_{zz} + \frac{1}{\epsilon} \frac{\kappa}{1 + \epsilon z \kappa} \partial_z + \frac{1}{1 + \epsilon z \kappa} \boldsymbol{\nabla}_s \cdot \left(\frac{1}{1 + \epsilon z \kappa} \boldsymbol{\nabla}_s \right), \tag{A9}$$

$$\partial_t = -\frac{\boldsymbol{n} \cdot \boldsymbol{u}}{\epsilon} \partial_z + o(1), \tag{A10}$$

where $\kappa = \boldsymbol{\nabla}_s \cdot \boldsymbol{n}$ is the total curvature of $\partial\Omega$. We assume that the inner expansion is given by

$$\hat{Y}(z, \boldsymbol{s}; \epsilon) = \hat{Y}^{(0)}(z, \boldsymbol{s}) + \epsilon \hat{Y}^{(1)}(z, \boldsymbol{s}) + \cdots, \tag{A11}$$

where $\hat{Y}$ represents $\hat{\boldsymbol{u}}$, $\hat{c}$, $\hat{\mu}$ and $\hat{p}$. In a region of overlap where both expansions are valid, we have

$$\bar{Y}_1(X + \epsilon z \boldsymbol{n}; \epsilon) \simeq \hat{Y}(z, \boldsymbol{s}; \epsilon) \quad \text{as } z \to -\infty, \tag{A12}$$

$$\bar{Y}_2(X + \epsilon z \boldsymbol{n}; \epsilon) \simeq \hat{Y}(z, \boldsymbol{s}; \epsilon) \quad \text{as } z \to +\infty. \tag{A13}$$

Combining (A 1), (A 11)–(A 13), we have the following asymptotic matching conditions at the first two leading orders:

$$\lim_{z \to -\infty} \hat{Y}^{(0)}(z, \boldsymbol{s}) = \bar{Y}_1^{(0)}(\boldsymbol{s}), \tag{A14}$$

$$\lim_{z \to -\infty} \hat{Y}^{(1)}(z, \boldsymbol{s}) = \bar{Y}_1^{(1)}(\boldsymbol{s}) + z \boldsymbol{n} \cdot \boldsymbol{\nabla} \bar{Y}_1^{(0)}, \tag{A15}$$

$$\lim_{z \to +\infty} \hat{Y}^{(0)}(z, \boldsymbol{s}) = \bar{Y}_2^{(0)}(\boldsymbol{s}), \tag{A16}$$

$$\lim_{z \to +\infty} \hat{Y}^{(1)}(z, \boldsymbol{s}) = \bar{Y}_2^{(1)}(\boldsymbol{s}) + z \boldsymbol{n} \cdot \boldsymbol{\nabla} \bar{Y}_2^{(0)}. \tag{A17}$$

Plugging the inner expansions into q-NSCH-DD and using (A 8)–(A 10), we derive the following inner equations at the leading order $\mathcal{O}(\epsilon^{-2})$:

$$\text{equation (3.1)} \to \tfrac{4}{3} \phi (\nu (\hat{\boldsymbol{u}}^{(0)} \cdot \boldsymbol{n})_z)_z - (1 - \phi)(\hat{\boldsymbol{u}}^{(0)} - \boldsymbol{u}_g) \cdot \boldsymbol{n} = 0, \tag{A18}$$

$$\text{equation (3.1)} \to \phi (\nu (\hat{\boldsymbol{u}}^{(0)} \cdot \boldsymbol{s})_z)_z - (1 - \phi)(\hat{\boldsymbol{u}}^{(0)} - \boldsymbol{u}_g) \cdot \boldsymbol{s} = 0, \tag{A19}$$

$$\text{equation (3.2)} \to \alpha \left(M(\hat{c}^{(0)}) \phi (\hat{\mu}^{(0)} + \alpha \hat{p}^{(0)})_z \right)_z = 0, \tag{A20}$$

$$\text{equation (3.3)} \to \left(M(\hat{c}^{(0)}) \phi (\hat{\mu}^{(0)} + \alpha \hat{p}^{(0)})_z \right)_z = 0, \tag{A21}$$

$$\text{equation (3.4)} \to -\epsilon_c^2 (\phi \hat{c}_z^{(0)})_z = 0. \tag{A22}$$

Note that the momentum (3.1) is expanded in both normal and tangential directions. Here we assume $\nu = 1$ for simplicity and obtain

$$\hat{\boldsymbol{u}}^{(0)} \cdot \boldsymbol{n} = \boldsymbol{u}_g \cdot \boldsymbol{n} + C_1 I_0 \left(\frac{\mathrm{e}^{3z}}{2\sqrt{3}} \right) + C_2 K_0 \left(\frac{\mathrm{e}^{3z}}{2\sqrt{3}} \right), \tag{A 23}$$

$$\hat{\boldsymbol{u}}^{(0)} \cdot \boldsymbol{s} = \boldsymbol{u}_g \cdot \boldsymbol{s} + C_3 I_0 \left(\frac{\mathrm{e}^{3z}}{3} \right) + C_4 K_0 \left(\frac{\mathrm{e}^{3z}}{3} \right), \tag{A 24}$$

$$(\hat{\mu}^{(0)} + \alpha \hat{p}^{(0)})_z = 0, \tag{A 25}$$

$$\hat{c}^{(0)} = C_5, \tag{A 26}$$

where C_* are constants, and I_0 and K_0 are the modified Bessel functions of the first and second kinds, respectively. Combining (A 23) and (A 24) with the leading-order matching conditions for $\boldsymbol{u}$ (A 14) and (A 16), we derive $\bar{\boldsymbol{u}}_1^{(0)} = \hat{\boldsymbol{u}}^{(0)} = \boldsymbol{u}_g$, and $C_5 = \bar{c}^{(0)}$.

At the next order of (3.2)–(3.4), $\mathcal{O}(\epsilon^{-1})$, we obtain

$$(\phi \boldsymbol{n} \cdot \hat{\boldsymbol{u}}^{(0)})_z - \boldsymbol{u}_g \cdot \boldsymbol{n} \phi_z = 0 = \alpha \left(M(\hat{c}^{(0)}) \phi (\hat{\mu}^{(1)} + \alpha \hat{p}^{(1)})_z \right)_z + \alpha \left(M(\hat{c}^{(1)}) \phi (\hat{\mu}^{(0)} + \alpha \hat{p}^{(0)})_z \right)_z, \tag{A 27}$$

$$\left(\phi M(\hat{c}^{(0)}) (\hat{\mu}^{(1)} + \alpha \hat{p}^{(1)})_z \right)_z = -\hat{\boldsymbol{u}}^{(0)} \cdot \boldsymbol{n} (\phi \hat{c}^{(0)})_z + \hat{\boldsymbol{u}}^{(0)} \cdot \boldsymbol{n} (\phi \hat{c}^{(0)})_z = 0, \tag{A 28}$$

$$(\phi \hat{c}_z^{(1)})_z = -\frac{\phi_z}{\epsilon_c \sqrt{2}} \cos(\theta)) \left(1 - \bar{c}^{(0)} \right) \bar{c}^{(0)}. \tag{A 29}$$

Integrating (A 28) and (A 29) both sides from $-\infty$ to $+\infty$ with respect to z, we have

$$\lim_{z \to -\infty} (\hat{\mu}^{(1)} + \alpha \hat{p}^{(1)})_z = 0, \tag{A 30}$$

$$\lim_{z \to -\infty} \hat{c}_z^{(1)} = \frac{1}{\epsilon_c \sqrt{2}} \cos(\theta) \left(1 - \bar{c}^{(0)} \right) \bar{c}^{(0)}. \tag{A 31}$$

Using the matching condition (A 15), we obtain

$$\boldsymbol{n} \cdot \nabla (\bar{\mu}_1^{(0)} + \alpha \bar{p}_1^{(0)}) = 0, \tag{A 32}$$

$$\boldsymbol{n} \cdot \nabla \bar{c}_1^{(0)} = \frac{1}{\epsilon_c \sqrt{2}} \cos(\theta) \left(1 - \bar{c}^{(0)} \right) \bar{c}^{(0)}. \tag{A 33}$$

Therefore, the outer solutions $\bar{\boldsymbol{u}}_1^{(0)}$, $\bar{\mu}_1^{(0)}$, $\bar{p}_1^{(0)}$ and $\bar{c}_1^{(0)}$ satisfy the original boundary conditions (2.38)–(2.40). Hence the q-NSCH-DD system recovers the q-NSCH model at leading order.

Appendix B. Numerical method and implementation

We now present a projection method for the q-NSCH-DD system (3.1)–(3.4) at the time-discrete level. Let $\mathrm{d}t > 0$ denote the time step, and assume $\boldsymbol{u}^n$, p^n, c^n and μ^n are

the solutions at time $t = n\,dt$. The solutions at time $t = (n + 1)\,dt$, namely $\boldsymbol{u}^{n+1}$, p^{n+1}, c^{n+1} and μ^{n+1}, are given by

$$\frac{\phi^{n+1}c^{n+1} - \phi^n c^n}{dt} + \nabla \cdot (\phi^n \boldsymbol{u}^n c^n) = \nabla \cdot \left(\phi^{n+1}M(c^{n+1})\nabla\mu^{n+1}\right)$$
$$+ \alpha\nabla \cdot \left(\phi^{n+1}M(c^{n+1})\nabla p^n\right), \qquad \text{(B 1)}$$

$$\phi^{n+1}\mu^{n+1} = \phi^{n+1}\epsilon_c F'(c^{n+1}) - \epsilon_c^2 \nabla \cdot (\phi^{n+1}\nabla c^{n+1})$$
$$- \frac{\epsilon_c |\nabla\phi^{n+1}|}{\sqrt{2}} \cos(\theta)\left(1 - c^{n+1}\right)c^{n+1}, \qquad \text{(B 2)}$$

$$\frac{\phi^{n+1}\rho^{n+1}\tilde{\boldsymbol{u}}^{n+1} - \phi^n\rho^n\boldsymbol{u}^n}{dt} + \rho^n\boldsymbol{u}^n \cdot \nabla(\phi^n\boldsymbol{u}^n)$$

$$= \phi^{n+1}\nabla \cdot \left(\nu^n\nabla\tilde{\boldsymbol{u}}^{n+1}\right) + \frac{\tilde{\sigma}}{\epsilon_c}\mu^{n+1}\nabla c^{n+1}$$

$$+ \frac{1}{3}\phi^{n+1}\nabla\left(\nu^n\nabla \cdot \tilde{\boldsymbol{u}}^{n+1}\right) - \frac{\left(1 - \phi^{n+1}\right)}{\epsilon^2}\left(\tilde{\boldsymbol{u}}^{n+1} - \boldsymbol{u}_g^{n+1}\right) - \phi^{n+1}\rho^{n+1}gz, \qquad \text{(B 3)}$$

$$dt\nabla \cdot \left(\frac{\phi^{n+1}}{\rho^{n+1}}\nabla p^{n+1}\right) = \nabla \cdot \left(\phi^{n+1}\tilde{\boldsymbol{u}}^{n+1}\right) - \boldsymbol{u}_g^{n+1} \cdot \nabla\phi^{n+1}$$

$$+ \alpha\nabla \cdot \left(\phi^{n+1}M(c^{n+1})\nabla\mu^{n+1}\right) + \alpha^2\nabla \cdot \left(\phi^{n+1}M(c^{n+1})\nabla p^{n+1}\right)$$

$$- dt\nabla \cdot \frac{\left(1 - \phi^{n+1}\right)}{\epsilon^2\rho^{n+1}}\left(\boldsymbol{u}^{n+1} - \tilde{\boldsymbol{u}}^{n+1}\right), \qquad \text{(B 4)}$$

$$\boldsymbol{u}^{n+1} = \tilde{\boldsymbol{u}}^{n+1} - \frac{\phi^{n+1}\nabla p^{n+1}}{\dfrac{\phi^{n+1}\rho^{n+1}}{dt} + \dfrac{\left(1 - \phi^{n+1}\right)}{\epsilon^2}}, \qquad \text{(B 5)}$$

with the following boundary conditions:

$$\tilde{\boldsymbol{u}}^{n+1}|_{\partial\tilde{\Omega}} = \boldsymbol{u}^{n+1}|_{\partial\tilde{\Omega}} = 0, \quad \boldsymbol{n} \cdot \nabla c^{n+1}|_{\partial\tilde{\Omega}} = \boldsymbol{n} \cdot \nabla(\mu^{n+1} + \alpha p^{n+1})|_{\partial\tilde{\Omega}} = 0. \qquad \text{(B 6}a,b\text{)}$$

Here we introduce a temporary velocity, $\tilde{\boldsymbol{u}}$, to split the original momentum (3.1). We first solve (B 1) and (B 2) to get c^{n+1} and μ^{n+1}, we then obtain $\tilde{\boldsymbol{u}}^{n+1}$ and p^{n+1} from (B 3) and (B 4). Finally the velocity $\boldsymbol{u}^{n+1}$ is updated in (B 5).

At the fully discrete level, our method uses a finite difference method on a staggered grid and implemented using an efficient, practical nonlinear multigrid solver, which was originally developed for solving a diffuse interface model for two-phase flows (Guo *et al.* 2017). In particular, we save the vector field, the velocity $\boldsymbol{u} = (u, v)$, as the edge-centred variables, and all the scalar variables c, μ, ϕ and p as the cell-centred variables. Here we use a regularized $\tilde{\phi} = \phi + \delta$, where $\delta = 10^{-6}$. The scheme is comprised of a standard FAS method for the Cahn–Hilliard equations (B 1) and (B 2), and a method based on the Vanka-type smoothing strategy for the Navier–Stokes equations (B 3)–(B 5). As demonstrated in Guo *et al.* (2017), the numerical method is first-order accurate in time and second-order accurate in space.

REFERENCES

ABELS, H., GARCKE, H. & GRUN, G. 2012 Thermodynamically consistent, frame indifferent diffuse interface models for incompressible two-phase flows with different densities. *Math. Models Meth. Appl. Sci.* **22** (03), 1150013.

AKI, G. L., DREYER, W., GIESSELMANN, J. & KRAUS, C. 2014 A quasi-incompressible diffuse interface model with phase transition. *Math. Models Meth. Appl. Sci.* **24** (05), 827–861.

ALAND, S., LOWENGRUB, J. & VOIGT, A. 2010 Two-phase flow in complex geometries: a diffuse domain approach. *Comput. Model. Engng Sci.* **57** (1), 77–106.

ANJOS, G., MANGIAVACCHI, N., BORHANI, N. & THOME, J. R. 2013 3D ALE finite-element method for two-phase flows with phase change. *Heat Transfer Engng* **35** (5), 537–547.

BIROS, G., YING, L. & ZORIN, D. 2004 A fast solver for the Stokes equations with distributed forces in complex geometries. *J. Comput. Phys.* **193** (1), 317–348.

BOYER, F. 2002 A theoretical and numerical model for the study of incompressible mixture flows. *Comput. Fluids* **31** (1), 41–68.

CAO, Z., SUN, D., WEI, J., YU, B. & LI, J. 2019 A coupled volume-of-fluid and level set method based on general curvilinear grids with accurate surface tension calculation. *J. Comput. Phys.* **396**, 799–818.

CHADWICK, A. F., STEWART, J. A., ENRIQUE, R. A., DU, S. & THORNTON, K. 2018 Numerical modeling of localized corrosion using phase-field and smoothed boundary methods. *J. Electrochem. Soc.* **165** (10), C633–C646.

CHEN, G., LI, Z. & LIN, P. 2007 A fast finite difference method for biharmonic equations on irregular domains and its application to an incompressible Stokes flow. *Adv. Comput. Maths* **29** (2), 113–133.

DE STEFANO, G., NEJADMALAYERI, A. & VASILYEV, O. V. 2016 Wall-resolved wavelet-based adaptive large-eddy simulation of bluff-body flows with variable thresholding. *J. Fluid Mech.* **788**, 303–336.

DING, H., SPELT, P. D. M. & SHU, C. 2007 Diffuse interface model for incompressible two-phase flows with large density ratios. *J. Comput. Phys.* **226** (2), 2078–2095.

DO-QUANG, M. & AMBERG, G. 2009 The splash of a solid sphere impacting on a liquid surface: numerical simulation of the influence of wetting. *Phys. Fluids* **21** (2), 022102.

DONG, S. & SHEN, J. 2012 A time-stepping scheme involving constant coefficient matrices for phase-field simulations of two-phase incompressible flows with large density ratios. *J. Comput. Phys.* **231** (17), 5788–5804.

DZIWNIK, M., MÜNCH, A. & WAGNER, B. 2017 An anisotropic phase-field model for solid-state dewetting and its sharp-interface limit. *Nonlinearity* **30**, 1465–1496.

FRANZ, S., ROOS, H.-G., GÄRTNER, R. & VOIGT, A. 2012 A note on the convergence analysis of a diffuse-domain approach. *Comput. Meth. Appl. Maths* **12** (2), 153–167.

FRIES, T. & BELYTSCHKO, T. 2010 The extended/generalized finite element method: an overview of the method and its applications. *Intl J. Numer. Meth. Engng* **84**, 253–304.

GAO, F., INGRAM, D. M., CAUSON, D. M. & MINGHAM, C. G. 2007 The development of a cartesian cut cell method for incompressible viscous flows. *Intl J. Numer. Meth. Fluids* **54** (9), 1033–1053.

GILMANOV, A. & SOTIROPOULOS, F. 2005 A hybrid Cartesian/immersed boundary method for simulating flows with 3d, geometrically complex, moving bodies. *J. Comput. Phys.* **207** (2), 457–492.

GLOWINSKI, R., PAN, T. W., HESLA, T. I., JOSEPH, D. D. & PÉRIAUX, J. 2001 A fictitious domain approach to the direct numerical simulation of incompressible viscous flow past moving rigid bodies: application to particulate flow. *J. Comput. Phys.* **169** (2), 363–426.

GONG, Y., ZHAO, J. & WANG, Q. 2017 An energy stable algorithm for a quasi-incompressible hydrodynamic phase-field model of viscous fluid mixtures with variable densities and viscosities. *Comput. Phys. Commun.* **219**, 20–34.

GONG, Y., ZHAO, J., YANG, X. & WANG, Q. 2018 Fully discrete second-order linear schemes for hydrodynamic phase field models of binary viscous fluid flows with variable densities. *SIAM J. Sci. Comput.* **40** (1), 138–167.

GRÁNÁSY, L., PUSZTAI, T., SAYLOR, D. & WARREN, J. A. 2007 Phase field theory of heterogeneous crystal nucleation. *Phys. Rev. Lett.* **98** (3).

GUO, Z. & LIN, P. 2015 A thermodynamically consistent phase-field model for two-phase flows with thermocapillary effects. *J. Fluid Mech.* **766**, 226–271.

GUO, Z., LIN, P. & LOWENGRUB, J. 2014a A numerical method for the quasi-incompressible Cahn–Hilliard–Navier–Stokes equations for variable density flows with a discrete energy law. *J. Comput. Phys.* **276**, 486–507.

GUO, Z., LIN, P., LOWENGRUB, J. & WISE, S. M. 2017 Mass conservative and energy stable finite difference methods for the quasi-incompressible Navier–Stokes–Cahn–Hilliard system: primitive variable and projection-type schemes. *Comput. Meth. Appl. Mech. Engng* **326**, 144–174.

GUO, Z., LIN, P. & WANG, Y. 2014b Continuous finite element schemes for a phase field model in two-layer fluid Bénard–Marangoni convection computations. *Comput. Phys. Commun.* **185** (1), 63–78.

GUTIÉRREZ, E., FAVRE, F., BALCÁZAR, N., AMANI, A. & RIGOLA, J. 2018 Numerical approach to study bubbles and drops evolving through complex geometries by using a level set–moving mesh–immersed boundary method. *Chem. Engng J.* **349**, 662–682.

HERRMANN, M. 2008 A balanced force refined level set grid method for two-phase flows on unstructured flow solver grids. *J. Comput. Phys.* **227** (4), 2674–2706.

HOHENBERG, P. C. 1977 Theory of dynamic critical phenomena. *Rev. Mod. Phys.* **49** (3), 435–479.

HU, H., PATANKAR, N. A. & ZHU, M. Y. 2001 Direct numerical simulations of fluid–solid systems using the arbitrary Lagrangian–Eulerian technique. *J. Comput. Phys.* **169** (2), 427–462.

JACQMIN, D. 1999 Calculation of two-phase Navier-Stokes flows using phase-field modeling. *J. Comput. Phys.* **155** (1), 96–127.

JIANG, Y., LIN, P., GUO, Z. & DONG, S. 2015 Numerical simulation for moving contact line with continuous finite element schemes. *Commun. Comput. Phys.* **18** (01), 180–202.

KIRKPATRICK, M. P., ARMFIELD, S. W. & KENT, J. H. 2003 A representation of curved boundaries for the solution of the Navier–Stokes equations on a staggered three-dimensional Cartesian grid. *J. Comput. Phys.* **184** (1), 1–36.

LERVAG, K. Y. & LOWENGRUB, J. 2015 Analysis of the diffuse-domain method for solving PDES in complex geometries. *Commun. Math. Sci.* **13** (6), 1473–1500.

LI, X., LOWENGRUB, J., RÄTZ, A. & VOIGT, A. 2009 Solving PDES in complex geometries: a diffuse domain approach. *Commun. Math. Sci.* **7** (1), 81–107.

LI, Z. 2003 An overview of the immersed interface method and its applications. *Taiwan. J. Math.* **7** (1), 1–49.

LIU, C. & WU, H. 2019 An energetic variational approach for the Cahn–Hilliard equation with dynamic boundary condition: model derivation and mathematical analysis. *Arch. Rat. Mech. Anal.* **233** (1), 167–247.

LIU, H. R. & DING, H. 2015 A diffuse-interface immersed-boundary method for two-dimensional simulation of flows with moving contact lines on curved substrates. *J. Comput. Phys.* **294**, 484–502.

LOWENGRUB, J. & TRUSKINOVSKY, L. 1998 Quasi-incompressible Cahn–Hilliard fluids and topological transitions. *Proc. R. Soc. Lond.* A **454** (1978), 2617–2654.

MITTAL, R., DONG, H., BOZKURTTAS, M., NAJJAR, F. M., VARGAS, A. & VON LOEBBECKE, A. 2008 A versatile sharp interface immersed boundary method for incompressible flows with complex boundaries. *J. Comput. Phys.* **227** (10), 4825–4852.

O'BRIEN, A. & BUSSMANN, M. 2018 A volume-of-fluid ghost-cell immersed boundary method for multiphase flows with contact line dynamics. *Comput. Fluids* **165**, 43–53.

POULSEN, S. O. & VOORHEES, P. W. 2018 Smoothed boundary method for diffusion-related partial differential equations in complex geometries. *Intl J. Comput. Meth.* **15** (3).

RAINER, B., STEVEN, M. W., MARCO, S. & AXEL, V. 2019 Convexity splitting in a phase field model for surface diffusion. *Intl J. Numer. Anal. Model.* **16** (2), 192–209.

SCHNEIDER, K. 2015 Immersed boundary methods for numerical simulation of confined fluid and plasma turbulence in complex geometries: a review. *J. Plasma Phys.* **81** (6).

SHIROKOFF, D. & NAVE, J.-C. 2014 A sharp-interface active penalty method for the incompressible Navier–Stokes equations. *J. Sci. Comput.* **62** (1), 53–77.

SHOKRPOUR ROUDBARI, M., ŞIMŞEK, G., VAN BRUMMELEN, E. H. & VAN DER ZEE, K. G. 2018 Diffuse-interface two-phase flow models with different densities: a new quasi-incompressible form and a linear energy-stable method. *Math. Models Meth. Appl. Sci.* **28** (04), 733–770.

STEIN, D. B., GUY, R. D. & THOMASES, B. 2017 Immersed boundary smooth extension (IBSE): a high-order method for solving incompressible flows in arbitrary smooth domains. *J. Comput. Phys.* **335**, 155–178.

TRYGGVASON, G., BUNNER, B., ESMAEELI, A., JURIC, D., AL-RAWAHI, N., TAUBER, W., HAN, J., NAS, S. & JAN, Y.-J. 2001 A front-tracking method for the computations of multiphase flow. *J. Comput. Phys.* **169** (2), 708–759.

YU, F., GUO, Z. & LOWENGRUB, J. 2020 Higher-order accurate diffuse-domain methods for partial differential equations with Dirichlet boundary conditions in complex, evolving geometries. *J. Comput. Phys.* **406**, 109174.

YU, H., CHEN, H. & THORNTON, K. 2012 Extended smoothed boundary method for solving partial differential equations with general boundary conditions on complex boundaries. *Model. Simul. Mater. Sci. Engng* **20** (7), 075008.

DE ZÉLICOURT, D., GE, L., WANG, C., SOTIROPOULOS, F., GILMANOV, A. & YOGANATHAN, A. 2009 Flow simulations in arbitrarily complex cardiovascular anatomies – an unstructured Cartesian grid approach. *Comput. Fluids* **38** (9), 1749–1762.

ZHANG, J. & NI, M. 2014 A consistent and conservative scheme for MHD flows with complex boundaries on an unstructured Cartesian adaptive system. *J. Comput. Phys.* **256**, 520–542.

ZHANG, Z. L., WALAYAT, K., CHANG, J. Z. & LIU, M. B. 2018 Meshfree modeling of a fluid-particle two-phase flow with an improved SPH method. *Intl J. Numer. Meth. Engng* **116** (8), 530–569.

ZHANG, Q. & WANG, X. 2016 Phase field modeling and simulation of three-phase flow on solid surfaces. *J. Comput. Phys.* **319**, 79–107.

ZOLFAGHARI, H., IZBASSAROV, D. & MURADOGLU, M. 2017 Simulations of viscoelastic two-phase flows in complex geometries. *Comput. Fluids* **156**, 548–561.